



Double surface rupture and hydraulic recharge of a three-fault system during the Mw 4.9 earthquake of 11 November 2019 at Le Teil (France)

André Burnol, Antoine Armandine Les Landes, Daniel Raucoules, Michael Foumelis, Cécile Allanic, Fabien Paquet, Julie Maury, Hideo Aochi, Théophile Guillon, Mickaël Delatre, et al.

► To cite this version:

André Burnol, Antoine Armandine Les Landes, Daniel Raucoules, Michael Foumelis, Cécile Allanic, et al.. Double surface rupture and hydraulic recharge of a three-fault system during the Mw 4.9 earthquake of 11 November 2019 at Le Teil (France). 2022. hal-03754409

HAL Id: hal-03754409

<https://brgm.hal.science/hal-03754409>

Preprint submitted on 24 Aug 2022

HAL is a multi-disciplinary open access archive for the deposit and dissemination of scientific research documents, whether they are published or not. The documents may come from teaching and research institutions in France or abroad, or from public or private research centers.

L'archive ouverte pluridisciplinaire **HAL**, est destinée au dépôt et à la diffusion de documents scientifiques de niveau recherche, publiés ou non, émanant des établissements d'enseignement et de recherche français ou étrangers, des laboratoires publics ou privés.



Distributed under a Creative Commons Attribution - NonCommercial 4.0 International License

1 Double surface rupture and hydraulic recharge of a three-fault
2 system during the Mw 4.9 earthquake of 11 November 2019 at Le
3 Teil (France)

4
5 André Burnol^{1*}, Antoine Armandine Les Landes¹, Daniel Raucoules¹,
6 Michael Foumelis^{1,2}, Cécile Allanic¹, Fabien Paquet¹, Julie Maury¹, Hideo
7 Aochi¹, Théophile Guillon¹, Mickael Delatre¹, Pascal Dominique¹, Adnand
8 Bitri¹, Simon Lopez¹, Philippe P. Pébay³, Behrooz Bazargan-Sabet¹

9 1. BRGM, 3 avenue Claude Guillemin, BP 36009, 45000 Orléans, France

10 2. Aristotle University of Thessaloniki (AUTH), School of Geology, Thessaloniki

11 3. Eredio, 28 rue de la Plane, 84330 Le Barroux

12
13 *Corresponding Author.

14 Email: a.burnol@brgm.fr

15
16
This manuscript is a non-peer reviewed preprint submitted
to EarthArXiv and to Communications Earth & Environment.
Please feel free to contact the corresponding author
a.burnol@brgm.fr ; we welcome feedback

Abstract

The Mw 4.9 earthquake of 11 November 2019 at Le Teil (France) occurred at a very shallow depth (about 1 km) inducing the surface rupture of La Rouvière fault, nearby of a limestone quarry. Thanks to satellite differential interferometry, we detected the existence of the secondary surface rupture of the quasi-parallel Bayne Rocherenard fault. A newly processed seismic cross-section allowed us to construct a local 3D fault system. Assuming that the earthquake was triggered by the transient increase in hydraulic pressure following heavy rainfall before the event, our numerical 3D simulations demonstrate that the hydraulic pressure gradient is maximum just before the earthquake at the intersection of the two faults, the most probable place of the hypocenter. This hydraulic effect is about two and a half times larger than the cumulative effect of mechanical stress release due to the mass removal from the surface quarry over the two past centuries.

1. Introduction

Large earthquakes usually occur along preexisting faults and plate interfaces. However, intraplate earthquakes are difficult to assess, as many damaging earthquakes are not associated to the known major faults, which were considered as the highest seismic potential in the area¹. Because the recurrence time of intraplate events is long, our knowledge and understanding of the fault dynamics (structure, rheology, stress loading and interaction) are still limited and causes other than the long-term tectonic stress loading are therefore considered for some earthquakes. For example, the 2008 Mw 7.9 Wenchuan (China) earthquake has a total fault length of more than 200 km in Longmenshan fault zone. Before the occurrence of the earthquake, the highest seismic potential of the area had never been attributed to the ruptured faults (causal faults) from the seismic hazard assessment² view point. Although the tectonic stress loading is undoubtable over the whole area, the nucleation process of this mega earthquake has been discussed in relation to the near-by Zipingpu reservoir in terms of the

elastic stress change and pore pressure change³⁻⁸. Indeed, any positive perturbation of stress on a causal fault can be suspected in triggering an earthquake⁹. The lack of *in situ* measurements does not allow however any definitive conclusion; the impoundment of the reservoir may have activated the shallow micro-seismicity within a few kilometers below the dam^{5,6} but the link to the hypocenter of the earthquake more than 10 km away is not clear.

The anthropogenic influence on earthquake triggering has been widely studied and several authors produced overview of the likely cases¹⁰⁻¹⁵, covering a range of magnitude between 1 and 8. At a local scale, the microseismicity at Gardanne, southern France is correlated to the flooding of the underground abandoned mining gallery with a time lag of about ten days¹⁶. The driving mechanism behind triggering is not only human-driven but can also be related to natural variations on the Earth's surface, namely climate variations¹⁷⁻¹⁹. It is reported that the seismicity in Himalaya has a seasonal trend according to the annual monsoon season, namely large amounts of precipitation in the summer^{20,21}. Among the studies analyzing the rainfall effect, the seasonal pore pressure evolution was discussed through fluid diffusion in the limestone of southeastern Germany¹⁹. The seismicity triggered by rainfall in karstic domain, in Switzerland, was studied through a fluid diffusion model in poro-elastic context²². The hypothesis of "hydroseismicity" developed by John K. Costain²³⁻²⁶ attributes most intraplate and near-intraplate earthquakes to the dynamics of the hydrologic cycle. Such hydraulic perturbations may occur from a few kilometers to 10 km away if a permeably connected fault system exists. In France, a correlation between heavy rainfall and small earthquakes was shown in the Western Provence around the Nîmes Fault²⁷ and in the Provence Alps at Castellane²⁸.

The 2019 Mw4.9 Le Teil (France) earthquake heavily damaged nearby

74 areas²⁹. Regardless of its moderate magnitude, this earthquake ruptured the
75 shallowest part of the known fault (only the first 2 km depth at most) and showed
76 rupture traces on the ground surface (Figure 1). The area had been known with
77 some historical earthquakes; however, earthquakes of this magnitude with surface
78 ruptures had never been taken into account in local/regional seismic hazard
79 assessment^{30,31}. As a first analysis, some authors pointed out that a nearby
80 limestone quarry may have contributed to the stress loading on the causal fault³²⁻
81 ³⁴. Using the seismograms available from the mainshock and aftershocks, Delouis
82 *et al.* (2021) shows that the best inferred epicenter is probably located not inside
83 but rather southwest of the surface quarry³⁵. Conversely, we investigate in this
84 work the so-called "hydraulic triggering hypothesis". Indeed, the studied area
85 suffered heavy rainfall during the month before the seismic event. Therefore, a
86 permeably connected fault system may play a role of conducting the pore pressure
87 change at depth. We focus on the local hydraulic system in the study area derived
88 from an updated regional geological model. The movement of moisture in partially-
89 saturated media is simulated using a 3D diphasic flow double permeability model
90 with the soil moisture data recorded during the period 2010-2019 as surface
91 boundary and the Rhône river as edge boundary conditions. We then discuss the
92 possible triggering mechanism by comparing the results of the hydraulic model
93 with those of a 3D mechanical model that simulates the mass withdrawal due to
94 the quarry exploitation in a similar geological configuration. We try to answer two
95 essential questions: (1) How large is the hydraulic overpressure due to the
96 meteoric water recharge vs. the Coulomb stress change due to the mass
97 withdrawal from the surface quarry? (2) Is the estimated location of the maximum
98 hydraulic overpressure consistent with the estimated hypocenter location?

2. Results

2.1. Geological and hydraulic context around the fault system

First, we collect the prior information on the fault system around Le Teil, independently of its co-seismic rupture process. The concerned area is located in the Rhône Valley in Southeastern France near the Montélimar city. The Urgonian limestones that are extracted from the nearby quarry were deposited in the early cretaceous epoch, during the Upper Barremian–Lower Aptian age and, afterwards, some calcareous marlstones are deposited during the Aptian–Albian age, east of La Rouvière Fault (LRF) (Figure 1). The available geological map³⁶ of the studied area at a scale of 1:50 000 shows the existence of several, mostly NE-SW striking fault segments in the area. The observed surface rupture³⁰ is consistent with the portion of the already mapped La Rouvière fault (LRF). The geometry of each segment of the geological map is studied through the differential SAR interferometry (DInSAR) analysis using the available Sentinel-1 images. The interpretation of seismic cross section is presented in the next section.

The hydraulic parameters in the Barremian limestones are highly variable. The continuous medium (“matrix”) and the “fault” elements are characterized by a large range of porosity and permeability^{37,38} (Table 1). For the “matrix”, we use a permeability of 10^{-16} m^2 and a porosity of 20% corresponding to the average values measured in the Low Noise Underground Laboratory (LSBB) (<https://lsbb.cnrs.fr/>) in the host rock of Upper Barremian limestones (Urgonian facies)³⁷. For the “fault”, a homogeneous high fault permeability value of 10^{-11} m^2 (i.e. a hydraulic conductivity of $k \sim 10^{-4} \text{ m s}^{-1}$ at 500 m depth) and a mean fault porosity of 10% are chosen to explore the infiltration in a highly conductive, intensively fractured fault zone that is representative of fast fluid conduits in the shallow subsurface. Such high permeability values are expected in the porous

layers along the fault zones in the Upper Barremian/Urgonian limestones³⁸⁻⁴⁰. These hydraulic parameters are used in the reference simulations of our 3D double porosity double permeability model (Table 1).

2.2. Surface traces of the fault system using DInSAR

Spaceborne Differential SAR interferometry (DInSAR) has been widely used during the past decades to track land subsidence or uplift related to groundwater extraction or underground gas storage⁴¹. The same method has been also successfully used for identifying ruptures due to earthquakes and quantifying the co-seismic motion^{42,43}. We particularly aim to refine the location of ruptures with a particular interest on La Rouvière fault (LRF) and the surrounding ones mapped on the 1:50 000 geological maps³⁶. To carry out this analysis, four interferograms were produced using SAR data from the Sentinel-1 mission (Method section and Figures S1-S4). After visual analysis of the four produced interferograms set (Table S1), only track A059 has sufficient quality on the area of major deformation. The interpretation of this interferogram is shown in Figure 2. The final geocoded product has 15 m spatial sampling. While the main rupture along LRF is clearly identified on the A059 interferogram, a secondary rupture can be suspected from the pattern of the deformation at the extremities of the ruptured area (Figure 2c and 2d). This latter coincides mostly with the mapped Bayne Rocherenard Fault (BRF) in the south-western area of the studied area, and this continues in the north-eastern direction, always parallel to the LRF, after the intersection with the Paurière Fault (PF) (Figure 2e). The interferometric coherence is better on the south-western part of the BRF than on its north-eastern part (more black pixels in Figure 2e). Figure 3 compares the identified positions with the cartographic representation of the faults as well as the differential motion along the rupture

traces. The main rupture along LRF exhibits motion up to 14 cm in Line of Sight (LOS) in the central part of the rupture (points LRF5 to LRF14 between 1000-3000m), that is consistent with previous results³⁰. The differential motion along BRF is estimated up to 4 cm, about one third of the main motion along LRF (Figure 3). The south-western part along BRF (BRR1 to BRR10 between 2000-3800m distance) moved two times less (about 2 cm) than the north-eastern part (BRR11 to P8 between 3900-5400m). The LRF motion moved more on the central part of the rupture (points LRF5 to LRF14 between 1000-3000m). This interferogram interpretation suggests the re-positioning of the north-eastern part of BRF. Most of the surface rupture evidences documented in the field³⁰ are close to LRF on the geological map³⁶, but one of them is found near the point P7 along the fault trace in Figure 3a, consistent with our proposed north-eastern extension of BRF. To be consistent with DInSAR analysis, we need therefore to reconstruct the fault model in the area: the found trace of BRF does not intersect with LRF on the ground surface, and this fault remains secondary in terms of the differential displacement. The 3D geometry is presented in the next section using a newly processed seismic cross-section.

2.3. 3D geometry of the fault system using M201 cross-section

In order to clarify the possible connectivity of the two faults (LRF and BRF), we re-interpret the seismic cross-section (M201, available on www.minergies.fr), whose location is shown in Figures 1 and 3. This profile was acquired by CGG company during 1962-1963 and retreated in 2020 by BRGM after Le Teil earthquake. Our seismic interpretation⁴⁴ of the geological layers in Figure 4 is partly based on the Valvignères exploration well drilled in 1963 (BSS002ARWX well at <http://infoterre.brgm.fr/>, see location in Figure S6). Since our work aims to

study the hydraulic and mechanical influence from the ground surface, we only focus on the local shallow structure of the first 2 km depth and follow from west to east La Rouvière (LRF), Bayne Rocherenard (BRF) and Paurière (PF) faults (Figure 5). LRF is a south-east dipping fault, consistent with the focal mechanism and finite source inversions of Le Teil earthquake^{32,35}. The seismic cross-section indicates that BRF is branching from LRF and PF is branching further from BRF. The position of each fault on the ground surface allowed us to estimate the dip angles, supposing that the dip angles are approximatively constant (see Texts S1-3 in Supplementary Information). We found a true dip angle of 54° for LR and this value between 45° and 60° is consistent with previous works³⁰. This shapes the geometry of our model at a local scale. This model is derived from an updated 3D geological model at a regional-scale⁴⁴ (up to 100 km horizontally and down to 5 km depth).

The SC03 borehole drilled by the quarry owner near the point P0 of the new BRF trace (Figure 3a) provides us some additional evidences that support this 3D fault model. The SC03 core samples show indeed at 90.5 m depth a near-vertical natural fracture with calcite veins (Figure S5) and at 112.5 m depth the geological evidence for fluids overpressures with angular fragments organized in a jigsaw puzzle pattern. Both observations indicate a possible intersection of SC03 with the new north-eastern part of BRF (Supporting Information, see Text S3). Another interesting observation is that an important quantity of water was lost at 83 m depth during the SC03 geotechnical drilling in 2016 inside the Le Teil quarry perimeter (personal communication of the quarry owner LAFARGE CEMENTS). We infer that the BRF fault zone could form a drain along the fracture network leading to fault parallel flows.

2.4. Hydraulic simulations using ComPASS

The precipitation data are compared with the seismic events during the period 2010-2019 in a rectangular area of 50 km x 25 km around the Teil quarry (Figure S6). Seismic data are extracted from the French national RéNaSS catalogue and the rainfall is measured by the weather station at Montélimar (44.58°N, 4.74°E) (Figure S6). The three most intense rainfalls between 2010 and 2019 (4th May 2010, 4th November 2014, 24th October 2019) are followed by a seismic event in this restricted area, which occurs between 8 and 18 days after these rainy episodes (Figure S6). The same delay was observed in other studies within a similar carbonate geological context^{19,28}. However, the number of events in this comparison is quite limited (only 12) and a statistical analysis is therefore not possible. Using our re-constructed fault model, we estimate here the pressure variations at depth linked to the infiltration of meteoric water in the period preceding the earthquake of 11 November 2019. In order to exclude as much as possible the evapotranspiration and surface runoff contributions, we use the soil moisture data at 30 cm (SM30) instead of the rainfall data during the period 2015-2019 (Figure 6). In order to simulate the previous period between 2010 and 2015, we use also the surface soil moisture (SSM) data acquired by the SMOS satellite (Figures 6 and S6). These data (SM30 or SSM) are used as input for the nodes at the top surface of the domain, except for those that belongs to the Rhône river where a constant/fixed boundary condition is applied (see Method section). Figure 5 illustrates the model volume consisting of the reconstructed fault model including the three-fault system (LRF, BRF and PF) as well as two other dipping faults close to the Rhône River. We adopt a so-called hybrid dimensional model coupling a 3D model of the matrix with a 2D model in fault planes using ComPASS^{45,46} (Method section).

In the reference case noted Ref16, we assume a permeability of 10^{-18} m^2 in the surface Apto-Albian clayey layer (Figure 5b), that is about 100 times lower than Upper Barremian limestones layer due to the clay fraction (Table 1). Soil moisture data at 30 cm depth (SM30) are used over the period 2015-2019 (Figure 6). The date of 24th September 2019 corresponds to a relative minimum pressure during the period 2015-2019 (Figure 7d-e). The differential of pressure (ΔP) for the period preceding the earthquake (between 24th September 2019 and 11th November 2019) is shown in Figure 7a-b. A peak value of ΔP appears along the intersection line between BRF and LRF (Figure 7c) which is higher than the peak value along the intersection line between PF and LRF (Figure 7a). ΔP reaches the maximum value of 0.98 MPa (982 kPa or 9.8 bars) at $Y = 1963 \text{ m}$ (Figure 7c) near the junction of the three-fault system LRF, BRF and PF. The temporal evolution of the pressure at this node is shown in Figure 7d between Mai 2015 and December 2019, revealing that the pressure gradient is maximum during the period just before the earthquake of November 11, 2019 (red dot). Using the 10-day SSM products for descending overpasses starting from 2010, we demonstrate that this pressure gradient is also maximum just before the earthquake during all the decade 2010-2019 (Figure S6). Therefore, a maximum overpressure on LRF takes place near the junction of the three faults at around 1,200 m depth. We verify here that the intersections between two or multiple faults are the most probable location zones for the hypocenter of an earthquake triggered by a hydraulic recharge according to the "hydroseismicity" concept developed by Costein²⁵.

The simulation results are qualitatively stable since the surface moisture is transported principally by BRF to the depth and the peak of the pore pressure appears around the junction of the three faults. Another case called Ref20 corresponds to a simplified scenario with a homogeneous permeability of 10^{-16} m^2

in the matrix (Table 1). In that case, we obtain a differential pressure of about 0.975 MPa. This counterintuitively indicates that the surface clays does not play a predominant role in establishing the hydraulic overpressure on LRF at depth. If we use SSM instead of SM30, the maximum differential of pressure decreases to the value of 0.9 MPa (Table 1). This slight decrease of the simulated overpressure is consistent with the observation that the SMOS-CATDS products underestimate generally the *in situ* soil moisture at Berzème (Figure 6), as already reported in southern France by others⁴⁷ (average bias of -9.5 vol.%).

3. Discussion

Our simulations show that the pore pressure change may reach 0.98 MPa at a depth of around 1.2 km at the intersection of LRF and BRF. It is thus naturally questioned how this is significant comparing to the mechanical impact due to the mass removal at Le Teil historical quarry nearby. Prior analytical evaluation of Coulomb stress, based on Boussinesq solution in a homogeneous half-space elastic medium show variations of 0.15 to 0.2 MPa^{32,48}. It is important to note that the earlier amplitude value of about 1 MPa proposed by De Novellis et al. (2020) was later corrected⁴⁸. We perform new 3D numerical simulations using 3DECTM distinct-element code⁴⁹ to represent our improved geological model including discontinuities as well as lithology in a 3D medium. The spatial distributions of $\Delta\sigma_n$ and $\Delta\tau$ on LRF are shown in Figure 8c and Figure 8d, respectively (Method section). The variations of the Coulomb Failure Function (ΔCFF) show a maximum change of 0.25 MPa at around 1 km depth on LRF (Figure 8b), a value of the same order as the Boussinesq solution^{32,48}. When we look carefully at the LRF, one peak (0.25 MPa) exists above the intersection with BRF, while another peak (0.24 MPa) appears along the intersection of LRF and BRF, promoted by the plasticity of the

fault element. An important portion of shear stress on LRF is generated along the fault line between LRF and BRF (Figure 8d). The Coulomb stress change ΔCFF is simulated by 3DECTM on all the considered fault segments (Figure S7). The maximum value of ΔCFF among all the faults appears not on LRF but on BRF (0.39 MPa at maximum). It is worthy to note that the mechanical stress change can be larger around the intersection of LRF and BRF and that BRF is more favorably located than LRF in terms of the mechanical stress change. The Coulomb stress change $\Delta CFF = |\Delta\tau| - \mu\Delta\sigma_n$ should be compared to the hydraulic term $\mu\Delta P$ with ΔP of about 1 MPa and μ of 0.6 (Method section). The study highlights that the hydraulic term $\mu\Delta P$ (0.6 MPa) is about two and a half times larger than the mechanical stress change (0.24 MPa) due to the mass removal from the ground surface. Moreover, the mechanical unloading remains a long-term quasi-static process over nearly 200 years while the hydraulic effect is a dynamic process immediately preceding the earthquake nucleation.

Another important discussion point is the consistency of the multiple relocation approaches of the hypocenter location. The studied area had not been covered by a dense seismic network before the earthquake. The closest station of the permanent network is far from the source area by about 30 km (OGLP station in Résif; <https://seismology.resif.fr/>), thus the hypocenter location using any catalogue has a significant uncertainty of several km³¹. However, a local network was installed just after the seismic event and the hypocenter of the Le Teil earthquake has been recently relocated using multiple approaches³⁵ (e.g. calibration from aftershocks). The most probable hypocenter location is at (44.5188 N, 4.6694 E, and 1.3 km depth) with an error of about 500m. This epicenter position is very close to the surface projection of the intersection of LRF and BRF (Figures 8 and 9). It is also close to the projected locations of the

maximum overpressures of both Ref16 and Ref20 reference simulations. A nearby blast monitoring station CLAU recorded the mainshock (Figure 9). Although this short period sensor was *a priori* only calibrated for micro-vibrations of quarry blasts, we found that the first particle motion could bring some useful information after testing one known blast event (Method section and Figure S9). The azimuth and its associated uncertainty of the first wave arrival of the mainshock is estimated to $N164^{\circ}E \pm 16^{\circ}$ (Figure 9). This direction is also consistent with our suggested epicenter locations. Observing this accordance between the seismological analyses and our hydraulic- and mechanical- modeling, we suggest that the intersection of LRF and BRF might have played an important role for the nucleation process of the Le Teil earthquake. Furthermore, the same authors³⁵ address the question of the indetermination of the dip angle for the mainshock (between 40° and 65°). The causal fault system is perhaps more complex than one single fault (LRF). It is well known that the nucleation process of an earthquake may occur around the geometrical irregularity of a complex fault system⁵⁰⁻⁵². The steeper BRF (69° dip in our study) may therefore have played a role in both seismic events, the mainshock and the aftershock.

4. Conclusion: a hydraulic triggering mechanism

We developed here two separate numerical models and used a decoupled modeling approach to compare the potential mechanical and hydraulic triggering factors for the earthquake of 11 November 2019 at Le Teil (France). The 3D geometry of the fault system was reconstructed through the surface rupture evidences of BRF found by our DInSAR interpretation (in addition to LRF) and a newly processed local seismic cross-section. Using the soil moisture data in the studied zone during the decade between 2010 and 2019, we carried out hydraulic

numerical simulations in the three dimensional volume. The near-vertical BRF geometry could have serve as major drain of the strong rainfall during the month before the earthquake, thus increasing the pore pressure at depth so as to possibly trigger a very shallow earthquake on LRF. The pore pressure at depth becomes a local peak just before the 2019 Le Teil earthquake at the intersection of the two segments BRF and LRF, very close to the hypocenter location determined by other seismological studies³⁵. The estimated amplitude is close to 1 MPa, about four times more important than the normal stress change elastically loaded on the fault due to the mass removal of the quarry from the ground surface (Figure 8). This work thus suggests a hydraulic triggering mechanism at shallow depth on a network of faults under long-term tectonic stress loading. The hydraulic recharge of similar fault systems may be the scope of future works in order to improve the local seismic hazard assessment around sensitive areas.

5. Methods

Differential SAR Interferometry (DInSAR)

The displacements are estimated along the sensor's Line of Sight (LOS), which is the sensor-to-target direction. DInSAR measures the projection of real motion along the LOS and provides 1D displacement measurements. Those measurements are relative in space and time: they are spatially related to a reference point, and temporally to the date of the first available satellite acquisition. Four interferograms were produced using Sentinel-1 data (Table S1). The processing is based on the Gamma processing software (<https://gamma-rs.com>). In order to interpret these interferograms for identifying and quantifying surface ruptures, an unwrapping additional step is required. For this step, we used the Minimum Cost Flow (Constantini, 1998) procedure implemented in Gamma. Unwrapped AO59

interferogram is shown in Figure 2. The visual examination allows a first estimation of the LRF rupture location and the positions of the extremities of a candidate for the BRF rupture (Figure 3). In order to obtain additional candidates we added positions of faults from the 1:50 000 geological map (see Figure S1). These faults were imported in the tool for profiles stacking and displacement estimation included in the Cosei-corr software^{53,54}. Lateral profiles are automatically generated by the software perpendicularly to the fault candidate (20 on LRF and 20 + 3 added manually on BRF). Our objective is first to validate points on the fault candidate as reliable observations if significant differential motion between each side of the profile is observed and then to quantify this motion. In addition, if the “jump” on the displacement profile is not exactly on the candidate’s position this procedure allows to adjust the position by displacing the candidate accordingly to the jump’s position. Figure S2 illustrates the use of the tool on the south-west of the LRF. Finally, the obtained points are connected in order to obtain a continuous rupture trace. This proposed procedure was found to be sensitive enough for interpreting the initial interferometric information and the results obtained are in fairly good agreement with ground failure observations (Figure 2). Although it cannot be fully exhaustive (minor motions could be missed), this provides a good representation of the positions of the LRF and BRF and a quantification of their surface displacements have been proposed. Furthermore, some unwrapping issues can occur close to the ruptures for two main reasons. First, some sectors of the area have poor coherence because of possible surface changes occurred during the 6 days time-span due to the earthquake itself or due to the presence of locally vegetated land covers. Secondly, the observed motion on the ruptures is larger than quarter of wavelength (i.e. 14 mm). One noteworthy point is the fact that two parallel ruptures introduces a specific unwrapping issue (illustrated in Figure

S3). This may have influenced on the location and quantification of the rupture traces. Complements on the unwrapping issues can be found, for example, in Hanssen⁵⁵ and Raucoules *et al.*⁵⁶. For these reasons, it is important to compare/validate the interpretation of the interferogram in respect to the prior knowledge of faults (e.g. ground observations or boreholes). The consequence is that it introduces an ambiguity on the distribution of the measured slip between the two faults. This issue may explain the different results provided by Ritz *et al.* (2020)³⁰ using the same Sentinel-1 data (Figure S4). As this ambiguity cannot be resolved only on the basis of the interferometric information, we use therefore additional observations (surface ruptures evidences or/and cores of boreholes).

Hydraulic simulations by ComPASS using soil moisture data

- *Soil Moisture (SM30) data at the Berzème station (SMOSMANIA)*

The SMOSMANIA network (Soil Moisture Observing System - Meteorological Automatic Network Integrated Application) is based on the existing automatic weather station network of Meteo-France. The SMOSMANIA soil moisture data are freely available on the web site of the International Soil Moisture Network (<https://ismn.geo.tuwien.ac.at/en/>). The stations form a Mediterranean-Atlantic transect following the marked climatic gradient between the two coastlines. The average distance between two neighbouring stations is approximately 40 km which is consistent with the spatial resolution of remote sensing soil moisture products (e.g. SMOS). The station at Berzème is located at less than 15 km from Le Teil (Figure S6). The vegetation on these sites is made up of natural fallow land, cut once or twice a year. Since April 24, 2015, four soil moisture probes (ThetaProbe ML3) are installed per station at depths of 5, 10, 20 and 30 cm. The ThetaProbe is

a capacitance probe using the dielectric permittivity properties of the soil to estimate the volumetric soil moisture content. The data at depth of 30 cm (noted SM30) are used in the hydraulic simulations Ref16, Ref20 (Table 1) and Ref6 (Table S4). The water content or soil moisture content is the quantity of water contained in the soil. The normalized water content (or effective saturation Se) is depended on the volumetric water content SM30 (raw data), the residual water content θ_r (about 12% between 2015 and 2019 at the Berzème station) and the saturated water content equivalent to porosity ω (about 42% at 30 cm at the Berzème station):

$$Se = \frac{(SM30 - \theta_r)}{(\omega - \theta_r)}$$

- *SMOS Level 3 Surface Soil Moisture (SSM) Products*

The first satellite mission to focus primarily on the collection of soil moisture data was the European SMOS satellite that was successfully launched on the 2nd of November 2009 by ESA. The surface soil moisture data acquired by the SMOS satellite between 2010 and 2019 are used in the numerical modeling as boundary conditions for the whole nodes at the top surface, except for those belonging to the Rhône river. We use here the term Surface Soil moisture (SSM) to refer to the volumetric soil moisture in the first few centimeters (0–5 cm) of the soil. It must also be noted that ascending and descending overpasses are bound to show different values of the retrieved parameters that may not be always comparable, and they are, thus, retrieved separately. The SMOS Level 3 SSM products are downloaded through the website of the Centre Aval de Traitement des Données SMOS (CATDS, <https://www.catds.fr>). The data are presented over the Equal-Area Scalable Earth (EASE grid 2)²⁵ with a sampling of about 25 km x 25 km and the studied area is included in one grid cell called L2 (Figures 1a and S6). The CATDS

provides either a 10-day SSM product (that contains median, minimum and maximum values of soil moisture) or a 3-day product. The 3-day products for ascending overpasses are used between Mai 2015 and December 2019 (Figure 6) and the 10-day aggregated products for descending overpasses are used between March 2010 and December 2019 (Figure S6). As the residual water content θ_r is almost zero for SMOS acquisitions, the normalized water content (or effective saturation Se) depends only on the volumetric water content SSM and the porosity ω (about 50% at 5-10 cm in the studied area given by the Harmonized World Soil Database):

$$Se = \frac{SSM}{\omega}$$

- *Hydraulic parameters (matrix, fault)*

The hydraulic parameters in the Barremian / Urgonian limestones are highly variable in the host rock, the damaged zone and the core fault³⁷⁻⁴⁰. In the Urgonian carbonates at Russel (<https://lsbb.cnrs.fr/>, about 90 km southeast of Le Teil), the observations show the presence of discontinuities (joints, veins, faults and stylolites) that influence the hydraulic properties from core to reservoir scale³⁸: the porosity varies from 1% to 20% and the permeability varies in a range between 10^{-17} m^2 and 10^{-11} m^2 . These hydraulic parameters are used by the ComPASS platform^{45,46} (<https://github.com/BRGM/ComPASS>) for the reference cases (Table 1) and the sensitivity cases (Table S4).

- *ComPASS platform*

The ComPASS code is able to handle complex networks of fractures with intersecting for non-isothermal compositional multiphase Darcy flows. The so-called hybrid dimensional model couples a 2D model in fractures with a 3D model

in the matrix. The model is discretized using a fully implicit time integration combined with the Vertex Approximate Gradient (VAG) finite volume scheme which adapted to polyhedral meshes and anisotropic heterogeneous media. The fully coupled systems are assembled and solved in parallel using the Single Program Multiple Data (SPMD) paradigm with one layer of ghost cells. This strategy allows for a local assembly of the discrete systems. Simulations can be run on unstructured meshes including complex networks of fractures with intersecting, immersed and non-immersed fractures. The fully coupled systems are assembled and solved in parallel using the PETSc library and can be run on large computing clusters. An efficient preconditioner is implemented to solve the linear systems at each time step and each Newton type iteration of the simulation.

- *Mesh, time step, convergence, element number used by ComPASS*

The open-source software platform under LGPL license named SALOME (<http://www.salome-platform.org>) has been used to generate the mesh for the whole domain, in order to, ultimately, simulate fluid flows in the faulted region using the ComPASS platform. The platform relies on the MED format, an internal data model, which describes meshes and fields stored as sequences of Hierarchical Data Format 5 (HDF5) structures. It also takes distributed meshes into account, thus facilitating parallel computations. The geological units and faults (Figure 5) were meshed by a tetrahedral conformal meshing using the SALOME code. The unstructured mesh is composed of more than 140,000 tetrahedral elements where the mesh size has been constrained for specific boundary elements (top surface, faults, intersection of faults). The fault is meshed as a two-dimensional (2D) surface with triangular elements which are interconnected with the surrounding matrix using conformal meshing. The finest elements are localized at the fault top

(triangles side lengths around 18 m). The top surface of the domain is composed of triangles with side length of approximately 50 m as well as triangles at the intersection of faults. Then, the finest tetrahedrons are localized close to the top surface and around the faults while the mesh becomes coarser by moving away from faults and the top surface (where triangles have side lengths of more than 250 m). For each simulation and at each time step, the nonlinear system is solved using a Newton algorithm. The GMRES stopping criterion on the relative residual is fixed to 10^{-8} . The Newton solver is convergent if the relative residual is lower than 10^{-8} as well. For each simulation, the initial timestep is about one hour and the maximum timestep is one day.

- *Hydraulic model and numerical simulations by ComPASS*

The model domain is set for a dimension of 5 km by 4 km by 3.5 km. The top surface of the model corresponds to the elevation of the area. The domain is composed of the geological units and faults in the studied area (Figure 5). Each unit and fault is considered homogenous in porosity and permeability (e.g. the permeability of the Apto-albian geological unit, see table 1). As a preliminary step, the initial state of the hydraulic system, is achieved by performing a first simulation over a long period (about 100 years) to reach an equilibrium state in the unsaturated zone where a diphasic flow "air/water" is simulated. In the initial state, the whole domain is considered fully saturated with a hydrostatic pressure state. For the boundary conditions, two different Dirichlet conditions are considered for the nodes at the top surface. At the nodes which belong to the Rhône river, we fix a constant pressure (1 bar) and a constant saturation (0 for the gas saturation). At the other nodes of the top surface, the gas saturation is gradually increased over time from a fully saturated state until to reach 0.9 (corresponding to a water

saturation Se of 0.1). The “no flow” boundary condition is applied on the four lateral and bottom boundaries. In the unsaturated zone, the values of relative permeability are defined by the power law $K_{rw} = Se^2$ and $K_{ra} = (1 - Se)^2$ for the water and air phase, respectively. The capillary pressure function P_c is given by the Corey law $P_c = -b \times \ln(Se)$ with $b = 2 \times 10^5 \text{ Pa}$. This first step gives an initial state with an unsaturated zone in the upper part of the hydraulic model, at equilibrium with the Rhône river. In the second step, the effective water saturation Se is changed every three (or ten) days during the period between 2010 (or 2015) and the end of 2019 for all the nodes at the top surface (except for the Rhône river nodes for which a constant water saturation of 1 is fixed). The variations of the water saturation, occurring over time, results in pressure variations/pulses in both unsaturated and saturated zones. More specifically, an increasing of water saturation at the top of the model, which is related to rainfall events results in pressure variations from the surface towards greater depth.

Mechanical simulations by 3DECTM

To model the mechanical effect of mass withdrawal on different faults, we use the Distinct Element Method of 3DECTM code⁴⁹ (Version 5.2, Itasca Consulting Group Inc.) that explicitly handles discontinuities as mechanically active joints. The model size is set for a dimension of 19 km by 12 km by 6 km oriented N110°E to be aligned with principal deformation directions⁵⁷. A limit of the 3DECTM is that discontinuities are defined only by flat surfaces. Each mechanical fault in the model corresponds to the mean plane of the geological fault, constraining the geometry of LRF by the observed fault trace position and a dip of about 50°. We attribute Coulomb behavior to these faults and their properties given in Table S2 are chosen according to the values measured for discontinuities in Barremian shale in the

French Low Noise Underground Laboratory (<http://lsbb.eu>)⁵⁸. As far as the lithology is concerned, we extract three layers from the 3D geological model: the basement, the Upper Jurassic and the Hauterivian layer (Figures 5 and 8). The discretization using tetrahedral meshes was done directly within the 3DECTM, the mean edge length is 200 m and the mesh is refined around the ground surface of mass removal and the target faults using a mean edge length of 100 m (Figure S7). The model parameters of the porous elastic medium are summarized in Table S3. In the first step, we realize an initial equilibrium to account for the initial state consisting of a gravitational loading plus a tectonic loading. We assign stress boundary conditions to the model (Figure 8a). As there is very few constraints on stress values, we define a reference model with a maximal horizontal stress of $\sigma_H = 1.3\sigma_v$ and a minimal horizontal stress of $\sigma_h = 1.1\sigma_v$ where σ_v is the vertical principal axis (minimum) defined by confining pressure. The top of the model is at a reference level corresponding to the lowest point within the area. We apply forces on top of this model to account for the topography. For the area of the quarry, the topography is reconstructed from the topography of 1950 (Figure S8) and a homogeneous additional layer is added corresponding to the volume extracted between 1833 and 1950. The second step consists in modelling the effect of mass withdrawal. To do this, the forces on top of the model are relaxed in the area of the quarry. We have no detailed information on temporal evolution of the topography, and only two periods are considered for the quarry extraction, before and after 1950. The volume extracted for the first period 1833-1950 is not well known and estimated by the quarry owner to be around $4.8 \times 10^6 \text{ m}^3$. The area of the quarry is estimated by using the study of De Novellis *et al.*³⁴ and the volume extracted is supposed evenly distributed on the whole surface. The volume extracted for the second period corresponds to the difference between the

topography between 2019 and 1950 over the area of the whole quarry (Figure S8). Using this observed map, our estimation of this volume is about $34 \times 10^6 \text{ m}^3$. The density of the extracted mass is assumed 2500 kg/m^3 , corresponding to 12 and 85 million tons for the two periods, respectively. The Coulomb stress change is given by $\Delta CFF = |\Delta\tau| - \mu(\Delta\sigma_n - \Delta P)$, where $\Delta\tau$ and $\Delta\sigma_n$ are the shear and normal stress changes (positive in compression), μ the frictional coefficient (Table S2) and ΔP the differential of pressure. The direction of $\Delta\tau$ is taken to the maximum shear stress on the given fault geometry. The Coulomb stress change ΔCFF related to the mass withdrawal is estimated from the difference between the two equilibrium steps. The mass withdrawal generates a relaxing of normal stress on LRF as well as an increase of shear stress.

Seismological data analysis at Clauzel House (CLAU)

The data recorded at Clauzel House (CLAU) are made available to the scientific community by the quarry owner LAFARGE CEMENTS. The sensor is a three-component, short-period seismograph (sampling rate at 1056.4 Hz), installed in a private house to monitor the vibrations due the quarry blasts. The recorded data of the mainshock include visually unnatural jumps in velocity and this leads to unexpected level of acceleration. After visiting the station CLAU, we observed that the station have not been correctly fixed on the house floor and probably may have been impacted by the fall of miscellaneous objects around. Although the whole waveform may not be exploitable, the first movement at the beginning of the signals could be informative³⁵. In order to verify the correct polarity, we check the blast signal of the 25th September 2019 for which the origin is known (Ev1 in Figure 8). For the given records, we remove the linear trend, apply the Butterworth bandpass filter (order of 8) between 1 and 10 Hz and integrate once using the

software SeisGram2K Seismogram Viewer v7.0.0X10 (www.alomax.net) for data viewing and processing. Then, we exploit the particle motion for a selected time window manually (Figure S9). We obtain a back azimuth of $N98^{\circ}E \pm 20^{\circ}$ for the true value of $N111^{\circ}E$. Thus, the particle motion indicates approximatively the event direction with a margin of error of around 15° . We thus use the data from the same station to estimate the direction of the mainshock of the 11th November 2019 and its associated uncertainty.

Data availability

Acquisitions of Sentinel-1 satellite for DInSAR are provided by the European Space Agency (ESA, <https://sentinel.esa.int/web/sentinel/sentinel-data-access>). The *in situ* soil moisture data and SMOS surface soil moisture data are freely available on the web site of the International Soil Moisture Network (ISMN, <https://ismn.geo.tuwien.ac.at/en/>) and of the French ground segment for the Level 3 data (CATDS, <https://www.catds.fr/>), respectively. The datasets generated and/or analyzed in this work are available from the corresponding author on reasonable request.

Code availability

The code that is central to our conclusions is the multiphase flow simulator called ComPASS. It is an open platform using state of the art numerical schemes to discretize multiphase Darcian flows on generic unstructured meshes. The version used is freely available at the GitHub platform (<https://github.com/BRGM/ComPASS>).

References

1. Stein, S., Geller, R. J. & Liu, M. Why earthquake hazard maps often fail and what to do about it. *Tectonophysics* **562–563**, 1–25 (2012).
2. Klinger, Y., Ji, C., Shen, Z.-K. & Bakun, W. H. Introduction to the Special Issue on the 2008 Wenchuan, China, Earthquake. *Bulletin of the Seismological Society of America* **100**, 2353–2356 (2010).
3. Lei, X. Possible roles of the Zipingpu Reservoir in triggering the 2008 Wenchuan earthquake. *Journal of Asian Earth Sciences* **40**, 844–854 (2011).
4. Kerr Richard A. & Stone Richard. A Human Trigger for the Great Quake of Sichuan? *Science* **323**, 322–322 (2009).
5. Deng, K. *et al.* Evidence that the 2008 Mw 7.9 Wenchuan Earthquake Could Not Have Been Induced by the Zipingpu Reservoir. *Bulletin of the Seismological Society of America* **100**, 2805–2814 (2010).
6. Gahalaut, K. & Gahalaut, V. K. Effect of the Zipingpu reservoir impoundment on the occurrence of the 2008 Wenchuan earthquake and local seismicity. *Geophysical Journal International* **183**, 277–285 (2010).
7. Ge, S., Liu, M., Lu, N., Godt, J. W. & Luo, G. Did the Zipingpu Reservoir trigger the 2008 Wenchuan earthquake? *Geophysical Research Letters* **36**, (2009).
8. Tao, W., Masterlark, T., Shen, Z.-K. & Ronchin, E. Impoundment of the Zipingpu reservoir and triggering of the 2008 Mw 7.9 Wenchuan earthquake, China. *Journal of Geophysical Research: Solid Earth* **120**, 7033–7047 (2015).
9. Mulargia, F. & Bizzarri, A. Anthropogenic Triggering of Large Earthquakes. *Scientific Reports* **4**, 6100 (2014).
10. Gupta, H. K. A review of recent studies of triggered earthquakes by artificial water reservoirs with special emphasis on earthquakes in Koyna, India. *Earth-Science Reviews* **58**, 279–310 (2002).
11. McGarr, A., Simpson, D., Seeber, L. & Lee, W. Case histories of induced and triggered seismicity. *International Geophysics Series* **81**, 647–664 (2002).
12. Davies, R., Foulger, G., Bindley, A. & Styles, P. Induced seismicity and hydraulic fracturing for the recovery of hydrocarbons. *Marine and Petroleum Geology* **45**, 171–185 (2013).
13. Foulger, G. R., Wilson, M. P., Gluyas, J. G., Julian, B. R. & Davies, R. J. Global review of human-induced earthquakes. *Earth-Science Reviews* **178**, 438–514 (2018).
14. Aochi, H. & Burnol, A. Mechanism of the ML4.0 25 April 2016 earthquake in southwest of France in the vicinity of the Lacq gas field. *Journal of Seismology* vol. 22 1139–1155 (2018).
15. Aochi, H., Le Guenan, T. & Burnol, A. Developing subsurface energy exploitation strategies by considering seismic risk. *Petroleum Geoscience* vol. 23 298–305 (2016).
16. Dominique, P., Aochi, H. & Morel, J. Triggered Seismicity in a Flooded Former Coal Mining Basin (Gardanne Area, France). *Mine Water and the Environment* **41**, 317–334 (2022).
17. Saar, M. O. & Manga, M. Seismicity induced by seasonal groundwater recharge at Mt. Hood, Oregon. *Earth and Planetary Science Letters* **214**, 605–618 (2003).
18. Heki, K. Snow load and seasonal variation of earthquake occurrence in Japan. *Earth and Planetary Science Letters* **207**, 159–164 (2003).
19. Hainzl, S., Kraft, T., Wassermann, J., Igel, H. & Schmedes, E. Evidence for rainfall-triggered earthquake activity. *Geophysical Research Letters* **33**, (2006).

- 677 20. Bollinger, L. *et al.* Seasonal modulation of seismicity in the Himalaya of
678 Nepal. *Geophysical Research Letters* **34**, (2007).
- 679 21. Ader, T. J. & Avouac, J.-P. Detecting periodicities and declustering in
680 earthquake catalogs using the Schuster spectrum, application to Himalayan
681 seismicity. *Earth and Planetary Science Letters* **377–378**, 97–105 (2013).
- 682 22. Husen, S., Bachmann, C. & Giardini, D. Locally triggered seismicity in the
683 central Swiss Alps following the large rainfall event of August 2005. *Geophysical*
684 *Journal International* **171**, 1126–1134 (2007).
- 685 23. Costain, J. K., Bollinger, G. A. & Speer, J. A. Hydroseismicity: A Hypothesis
686 for The Role of Water in the Generation of Intraplate Seismicity. *Seismological*
687 *Research Letters* **58**, 41–64 (1987).
- 688 24. Costain, J. K. & Bollinger, G. A. Review: Research Results in
689 Hydroseismicity from 1987 to 2009. *Bulletin of the Seismological Society of*
690 *America* **100**, 1841–1858 (2010).
- 691 25. Costain, J. K. Groundwater recharge as the trigger of naturally occurring
692 intraplate earthquakes. *Geological Society, London, Special Publications* **432**, 91
693 (2017).
- 694 26. Costain, J. K. Finite element simulation of an intraplate earthquake
695 setting—Implications for the Virginia earthquake of 23 August 2011. *Geological*
696 *Society of America Special Papers* **509**, 137–150 (2015).
- 697 27. Rigo, A., Béthoux, N., Masson, F. & Ritz, J.-F. Seismicity rate and wave-
698 velocity variations as consequences of rainfall: The case of the catastrophic
699 storm of September 2002 in the Nîmes Fault region (Gard, France). *Geophysical*
700 *Journal International* **173**, 473–482 (2008).
- 701 28. Bollinger, L., Nicolas, M. & Marin, S. Hydrological triggering of the
702 seismicity around a salt diapir in Castellane, France. *Earth and Planetary Science*
703 *Letters* **290**, 20–29 (2010).
- 704 29. Causse, M. *et al.* Exceptional ground motion during the shallow Mw 4.9
705 2019 Le Teil earthquake, France. *Communications Earth & Environment* **2**, 14
706 (2021).
- 707 30. Ritz, J.-F. *et al.* Surface rupture and shallow fault reactivation during the
708 2019 Mw 4.9 Le Teil earthquake, France. *Communications Earth & Environment*
709 **1**, 10 (2020).
- 710 31. Cornou, C. *et al.* Rapid response to the $M_{\text{protect}} = 4.9$ earthquake of
711 November 11, 2019 in Le Teil, Lower Rhône Valley, France. *Comptes Rendus.*
712 *Géoscience* (2021) doi:10.5802/crgeos.30.
- 713 32. Ampuero, J. P. *et al.* Rapport d'évaluation du groupe de travail (GT) CNRS-
714 INSU sur le séisme du Teil du 11 novembre 2019 et ses causes possibles.
715 <https://hal.archives-ouvertes.fr/hal-03080941> (2019).
- 716 33. Larroque, C., Ampuero, J.-P., Delouis, B. & Cornou, C. Aux origines du
717 séisme du Teil. *La Recherche* **561**, 94–97 (2020).
- 718 34. De Novellis, V. *et al.* Coincident locations of rupture nucleation during the
719 2019 Le Teil earthquake, France and maximum stress change from local cement
720 quarrying. *Communications Earth & Environment* **1**, 20 (2020).
- 721 35. Delouis, B. *et al.* Constraining the point source parameters of the 11
722 November 2019 Mw 4.9 Le Teil earthquake using multiple relocation approaches,
723 first motion and full waveform inversions. *Comptes Rendus. Géoscience* (2021)
724 doi:10.5802/crgeos.78.
- 725 36. Y Kerrien, S Elmi, R. Busnardo, G. Camus, G. Kieffer, J. Moinereau, A.
726 Weisbrod. Carte géol. France (1/50000), feuille Aubenas (865). BRGM : Orléans.
727 Notice explicative par S. Elmi, R. Busnardo, B. Clavel, G. Camus, G. Kieffer, P.
728 Bérard, B. Michaëly (1996), 170 p. (1989).

37. Cochard, J. *et al.* Reservoir properties of barremian–aptian urgonian limestones, SE France, Part 1: influence of structural history on porosity-permeability variations. *Journal of Petroleum Geology* **43**, 75–94 (2020).
38. Jeanne, P., Guglielmi, Y., Lamarche, J., Cappa, F. & Marié, L. Architectural characteristics and petrophysical properties evolution of a strike-slip fault zone in a fractured porous carbonate reservoir. *Journal of Structural Geology* **44**, 93–109 (2012).
39. Guglielmi, Y., Cappa, F., Avouac, J.-P., Henry, P. & Elsworth, D. Seismicity triggered by fluid injection - induced aseismic slip. *Science* **348**, 1224–1226 (2015).
40. Aubert, I., Lamarche, J. & Léonide, P. Ternary fault permeability diagram: An innovative way to estimate fault zones hydraulics. *Journal of Structural Geology* **147**, 104349 (2021).
41. Burnol, A. *et al.* Wavelet-based analysis of ground deformation coupling satellite acquisitions (Sentinel-1, SMOS) and data from shallow and deep wells in Southwestern France. *Scientific Reports* vol. 9 8812 (2019).
42. Raucoules, D. *et al.* Validation and intercomparison of Persistent Scatterers Interferometry: PSIC4 project results. *Journal of Applied Geophysics* **68**, 335–347 (2009).
43. Massonnet, D. *et al.* The displacement field of the Landers earthquake mapped by radar interferometry. *Nature* **364**, 138–142 (1993).
44. Allanic, C. *et al.* Séisme du Teil (11.11.2019) : structuration géologique 3D du sous-sol. in *27e édition de la Réunion des Sciences de la Terre* (2021).
45. Xing, F., Masson, R. & Lopez, S. Parallel numerical modeling of hybrid-dimensional compositional non-isothermal Darcy flows in fractured porous media. *Journal of Computational Physics* **345**, 637–664 (2017).
46. Lopez, S. *et al.* Geothermal Modeling in Complex Geological Systems with the CompASS Code. in *Stanford Geothermal Workshop 2018-43rd Workshop on Geothermal Reservoir Engineering* (2018).
47. El Hajj, M. *et al.* Evaluation of SMOS, SMAP, ASCAT and Sentinel-1 Soil Moisture Products at Sites in Southwestern France. vol. 10 (2018).
48. De Novellis, V. *et al.* Author Correction: Coincident locations of rupture nucleation during the 2019 Le Teil earthquake, France and maximum stress change from local cement quarrying. *Communications Earth & Environment* **2**, 47 (2021).
49. Itasca. *3DEC—3 Dimensional Distinct Element Code v5.2*. (Itasca Consulting Group Inc., 2016).
50. Yoshida, S. *et al.* Joint Inversion of Near- and Far-field Waveforms and Geodetic Data for the Rupture Process of the 1995 Kobe Earthquake. *Journal of Physics of the Earth* **44**, 437–454 (1996).
51. Kaverina, A., Dreger, D. & Price, E. The Combined Inversion of Seismic and Geodetic Data for the Source Process of the 16 October 1999 Mw 7.1 Hector Mine, California, Earthquake. *Bulletin of the Seismological Society of America* **92**, 1266–1280 (2002).
52. Ozacar, A. A. & Beck, S. L. The 2002 Denali Fault and 2001 Kunlun Fault Earthquakes: Complex Rupture Processes of Two Large Strike-Slip Events. *Bulletin of the Seismological Society of America* **94**, S278–S292 (2004).
53. Leprince, S., Ayoub, F., Klinger, Y. & Avouac, J.-P. Co-registration of optically sensed images and correlation (COSI-Corr): An operational methodology for ground deformation measurements. in *2007 IEEE international geoscience and remote sensing symposium* 1943–1946 (IEEE, 2007).

54. Ayoub, F., Leprince, S. & Keene, L. User's guide to COSI-CORR co-registration of optically sensed images and correlation. *California Institute of Technology: Pasadena, CA, USA* **38**, 49s (2009).
55. Hanssen, R. F. *Radar interferometry: data interpretation and error analysis*. vol. 2 308 (Springer Science & Business Media, 2001).
56. Raucoules, D., Colesanti, C. & Carnec, C. Use of SAR interferometry for detecting and assessing ground subsidence. *Comptes Rendus Geoscience* **339**, 289–302 (2007).
57. Masson, C., Mazzotti, S., Vernant, P. & Doerflinger, E. Extracting small deformation beyond individual station precision from dense Global Navigation Satellite System (GNSS) networks in France and western Europe. *Solid Earth* **10**, 1905–1920 (2019).
58. Derode, B., Guglielmi, Y., De Barros, L. & Cappa, F. Seismic responses to fluid pressure perturbations in a slipping fault. *Geophysical Research Letters* **42**, 3197–3203 (2015).

Acknowledgments

This research was conducted as part of a research partnership co-funded by BRGM and the quarry owner LAFARGE CEMENTS (grants CF19DRP21 and CF21DRP01). We thank LAFARGE CEMENTS to make available the extracted volumes of rocks from Le Teil quarry during the period 1850-2019 and the data of the SC03 geotechnical borehole drilled in 2016. A.Bu warmly thanks his former PhD supervisor Laurent Charlet for the field visit looking for possible water sinkholes around the epicenter location and the visit of his nearby house at Saint-Thomé damaged by the earthquake.

Authors contributions

A.Bu and H.A wrote the main manuscript. A.Bu conceived the hydraulic study, performed the SMOS and Berzème station data processing and contributed to the overall interpretation. A.A.L performed the 3D hydraulic model with the ComPASS version developed by S.L and the post-processing with Paraview with the support of P.PB. M.F performed the overall SAR data processing with Gamma and D.R interpreted the unwrapped interferogram. J.M performed the mechanical 3D model with 3-DEC with the contribution of T.G and contributed with H.A and B.B.S to the interpretation of the mechanical results. A.Bi and F.P contributed respectively to the retreatment and interpretation of the seismic M201 profile. C.A performed the geological data analyses and construct the 3D structural model at regional scale. M.D, P.D and H.A performed the processing of the signal acquired by the vibration sensor CLAU. B.B.S conceived the global study. All authors contributed to the text and reviewed the manuscript.

Ethics declarations

The authors declare that they have no competing interests as defined by Nature Research. The research support of LAFARGE CEMENTS to BRGM (grants CF19DRP21 and CF21DRP01) did not include any role in the conceptualization, study design, data analysis, decision to publish, or preparation of the manuscript.

Supplementary information

Suppl_Info_V5

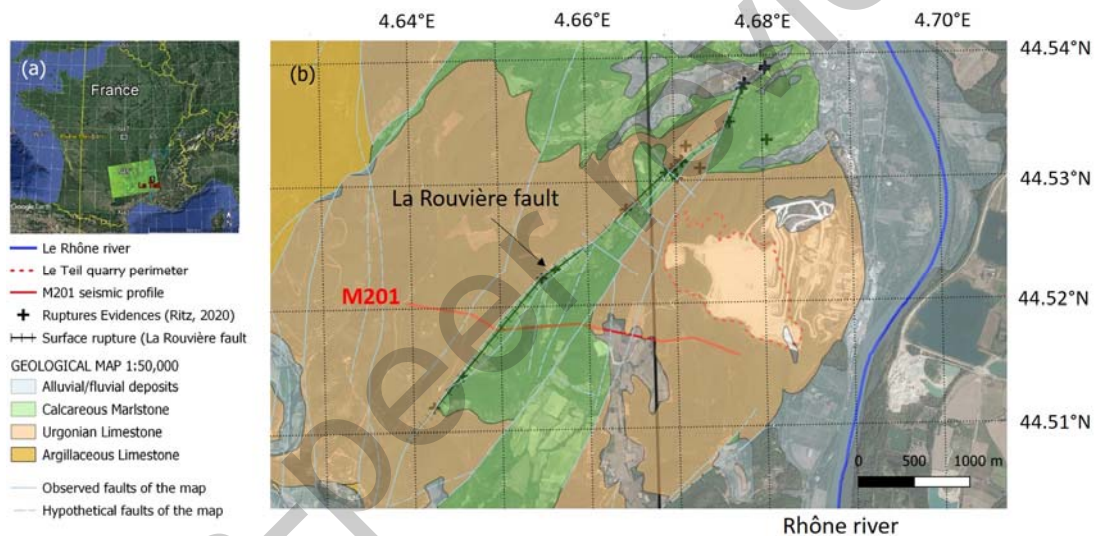
833 Table and Figures

834

835 Table 1 Hydraulic model simulations (parameters and results)

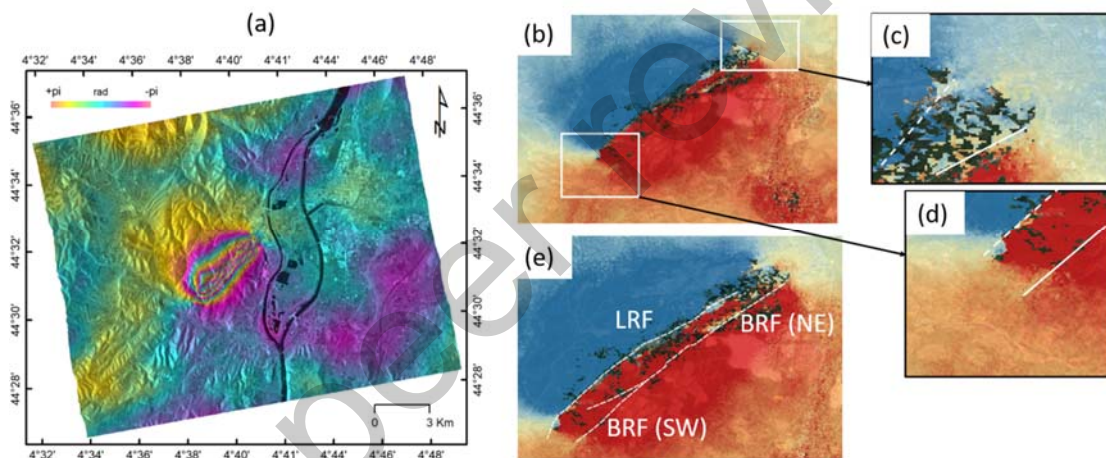
	Ref16	Ref20	Ref21
Soil moisture	SM30 (Berzème, 30 cm depth)	SM30 (Berzème, 30 cm depth)	SSM (SMOS ASC, 3 days)
Matrix Porosity w_m	0.2	0.2	0.2
Matrix Permeability K_m	10^{-18} m^2 in Apto-albien 10^{-16} m^2 elsewhere	10^{-16} m^2	10^{-18} m^2 in Apto-albien 10^{-16} m^2 elsewhere
Fault Porosity w_f	0.1	0.1	0.1
Fault Permeability K_f	10^{-11} m^2	10^{-11} m^2	10^{-11} m^2
Fault Width W	20 m	20 m	20 m
Maximum differential of pressure (ΔP) along the intersection LRF / BRF	9.82 bar	9.75 bar	9.03 bar

Figure 1: Map of the studied area. (a) Location of the studied area near Le Teil city in the southeastern France. Data are combined on Google map, Landsat/Copernicus, SIO, NOAA, US Navy, NGA and GEBCO and include one Copernicus Sentinel image (2019) that contains the 25 km SMOS L2 cell of the EASE equal-area grid (black square). (b) Simplified bedrock geology modified from the BRGM geological map at the 1:50,000 scale (Kerrien *et al.*, 1989) showing the observed faults (light blue solid lines) and hypothetical faults (light blue dashed lines). The surface trace of La Rouvière fault (LRF) (black line) is the black line joining the ruptures evidences (black crosses) of Ritz *et al.* (2020). Also shown the M201 seismic cross-section (solid red line), Le Teil quarry perimeter (dotted red line) and the north-south axis at around 4.67° , which is the boundary between L1 and L2 SMOS cells.



839

Figure 2. Double surface rupture using Sentinel-1 synthetic-aperture radar data. (a) A059 (Ascending mode) interferogram (wrapped phase) showing a fringe (phase variation of 2π) corresponding to a surface displacement of 28 mm in line of sight (LOS). The total movement is about 5.5 fringes (about 15 cm in LOS). (b) The unwrapping of A059 allows to convert the phases in LOS displacement of the Sentinel-1 satellite (viewing angle of 43.7°). The black pixels corresponding to pixels with insufficient coherence and are masked during the unwrapping process. (c)(d) Zooms on both extremities of the detected surface rupture (white lines). (e) Double surface rupture (white lines) of the main fault (La Rouvière; LRF) and the secondary fault (Bayne Rocherenard fault; BRF) including the new position of the North-East part (NE).



840

841

Figure 3: Distribution of surface displacements along the main and secondary faults. (a) Position of the surface rupture points (yellow circles and red shaded line) and interpretation in terms of fault traces showing two co-seismic rupture lines roughly parallel: the main La Rouvière fault (LRF between LRF1 and LRF20) and the secondary Bayne Rocherenard fault (BRF between BRR1 and BRR11, continuing farther between P0 and P11). Also shown are the previously mapped faults (Kerrien *et al.*, 1989) and the rupture evidences observed by Ritz *et al.* (2020). **(b)** Comparison of Line of Sight (LOS) displacements for LRF and BRF faults (starting points of both profiles are the most southwestern points LRF1 and BRR1, respectively).

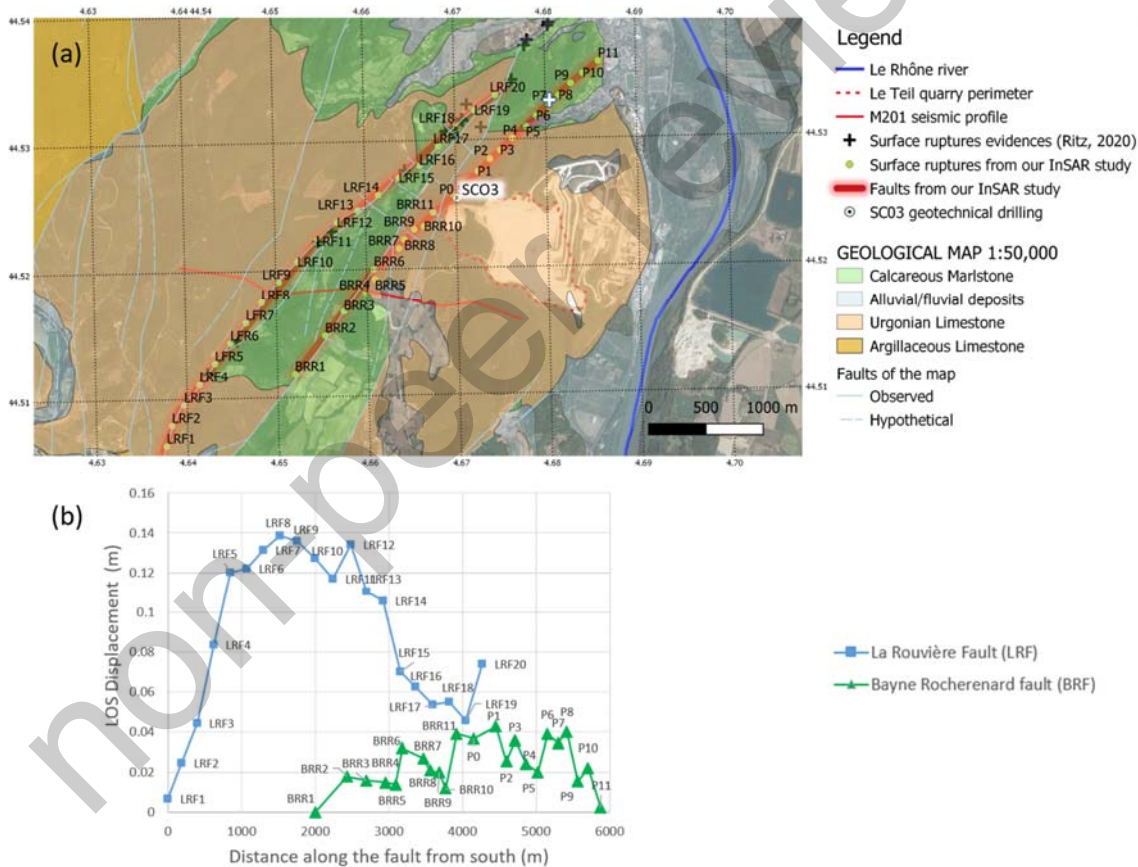
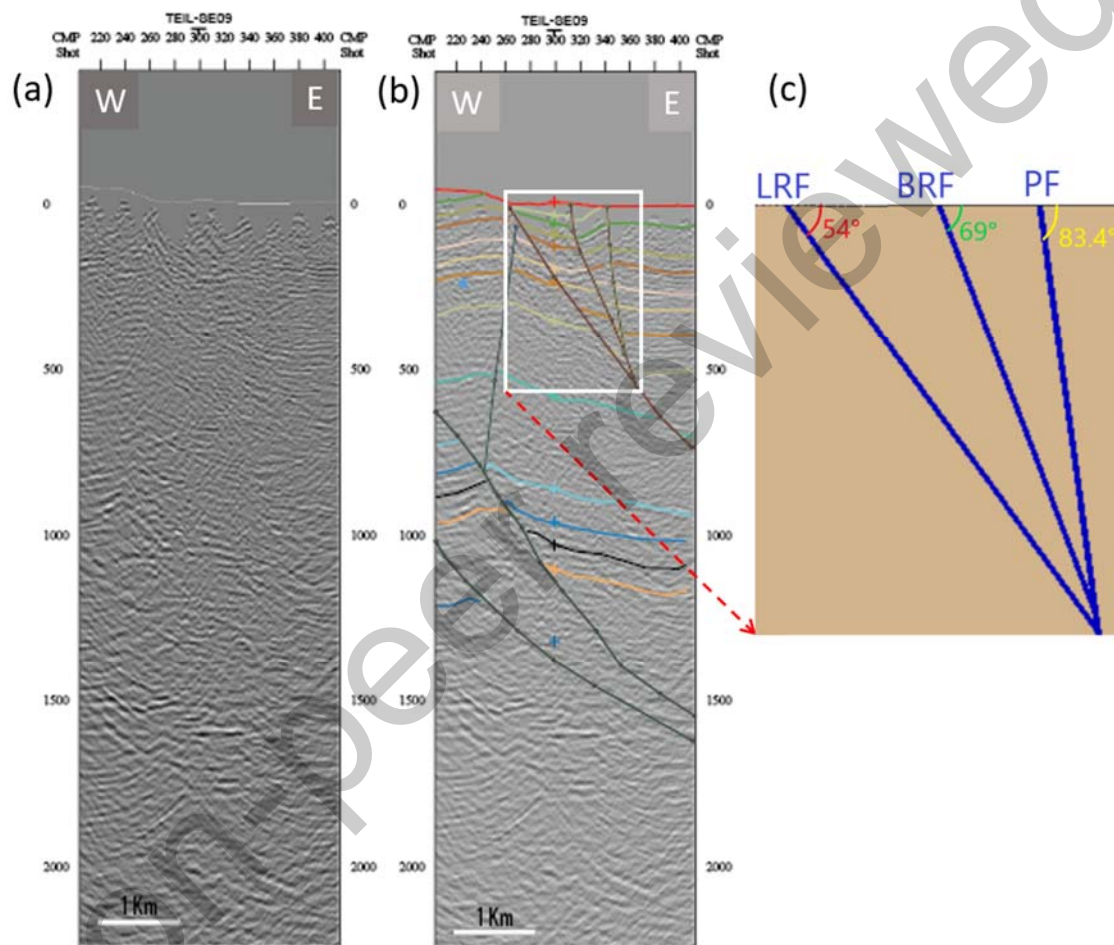


Figure 4. Interpretation of the seismic profile M201. (a) The data along the cross-section M201 in the time domain (vertical scale is two-way travel time). (b) Interpretation of the faults and geological layers on M201 consistent with our updated geological model. (c) True dip angles of LRF (La Rouvière), BRF (Bayne Rocherenard) and PF (Paurière) faults (see Supplementary information for our calculation method, texts S1-S3).



854 **Figure 5. Mesh of the hydraulic model. (a)** Three-fault system consisting of
 855 LRF (La Rouvière), BRF (Bayne Rocherenard) and PF (Paurière) faults. Two other
 856 faults in the East are also included. Also shown is the topographic surface with the
 857 Rhône river. (b) Matrix including, among other layers, the surface layer
 858 characterized by the Apto-Albian clay layer (green) and the Barremian limestones
 859 (the rest).

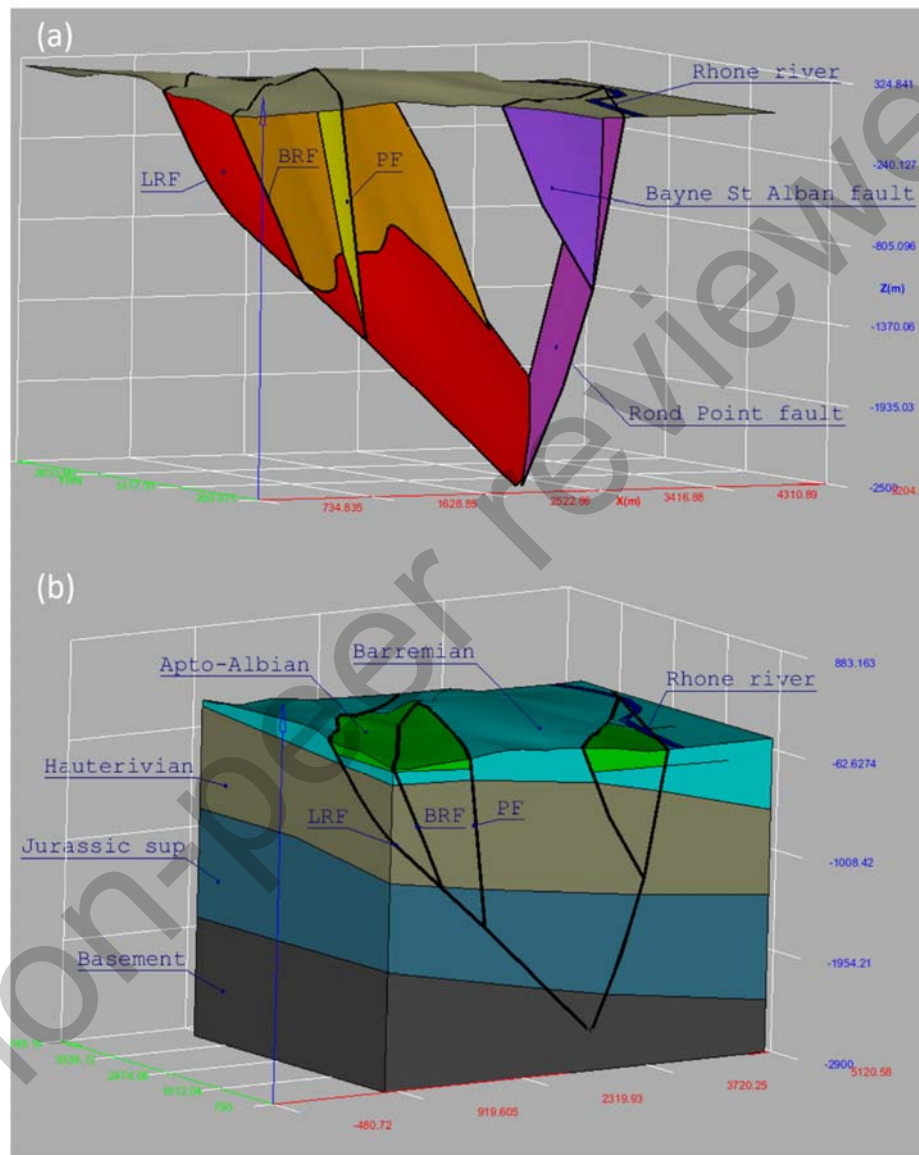


Figure 6. Surface boundary condition of the hydraulic model. The effective saturation S_e (also called normalized water content) is calculated using *in situ* soil moisture at 30 cm depth (SM30) at Berzème or Surface Soil Moisture (SSM) every 3 days or 10 days acquired by SMOS in the L2 cell (method section).

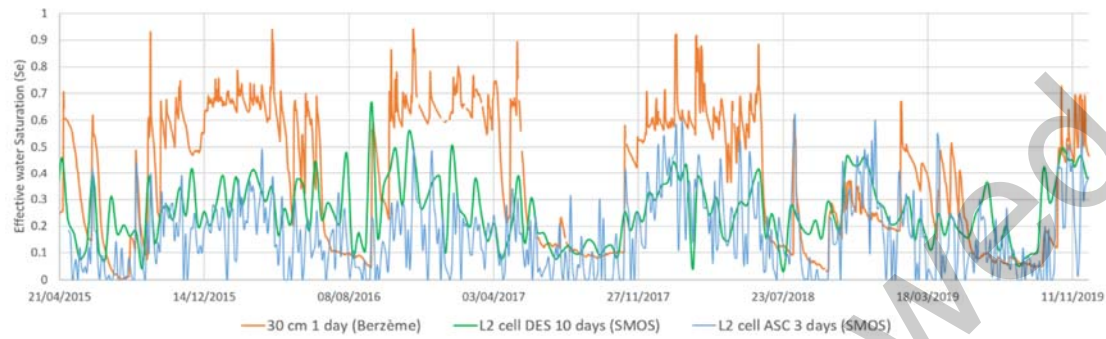


Figure 7. Simulation result for the reference case using the soil moisture at 30 cm (Ref16). (a) Differential of pressure (ΔP) on LRF between 11th November 2019 and 24th September 2019. The intersection of BRF (or PF) with LRF is indicated by a grey (or white) dotted line. (b) ΔP on the local fault system (same view as in Figure 5). (c) Spatial variation of ΔP along the intersection line between LRF and BRF. Red diamond is the position of the node along this line where ΔP is maximum. (d) Temporal pressure variation between 2015 and 2019 at the node where ΔP is maximum (blue line) and the pressure gradient for the previous 30 days (dotted grey line). The filled green square indicates the relative pressure minimum on 24th September 2019. The filled red circle indicates the pressure on 11th November 2019. (e) Zoom of (d) during the year 2019. Also shown is the result of the Ref21 case using the surface soil moistures (SSM).

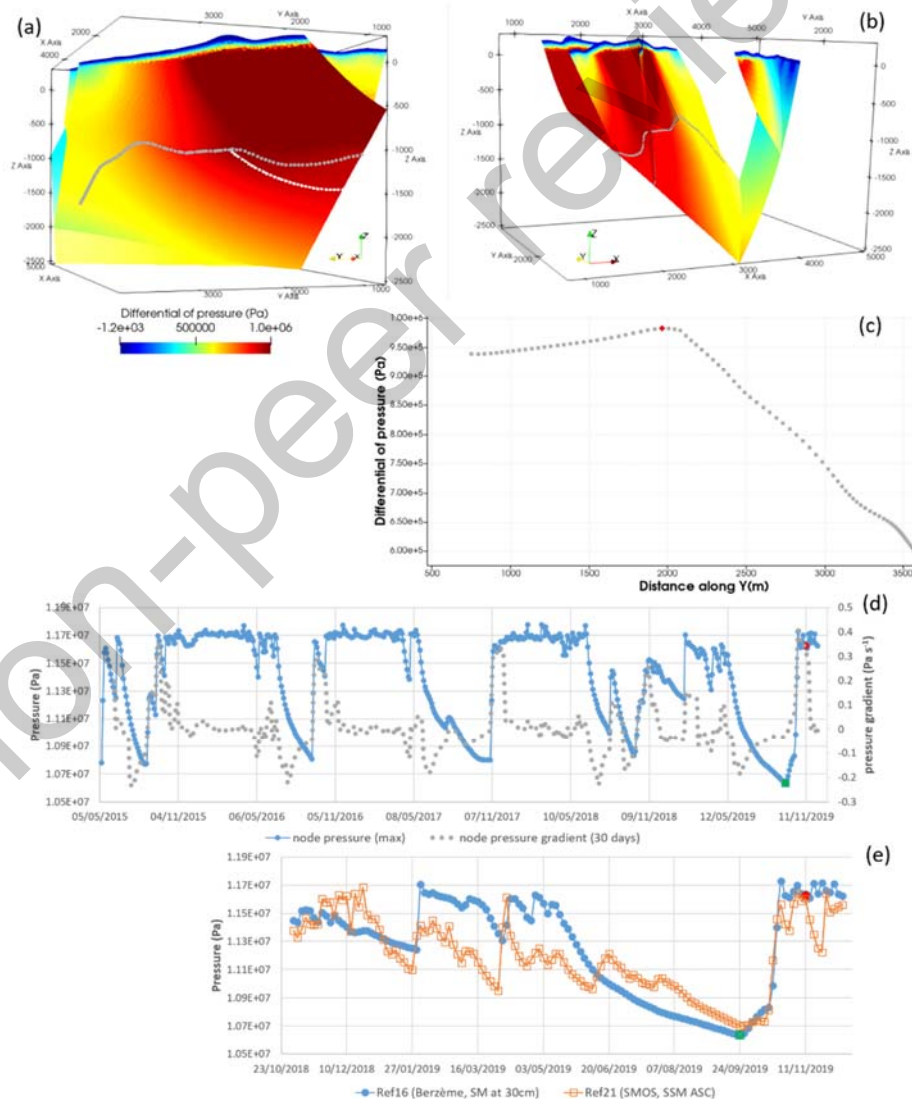


Figure 8. Mechanical simulation by 3DEC™. (a) Conception of the mechanical model (change of the topography is given by a change of force on the ground surface). (b) Coulomb stress change (ΔCFF) on LRF related to mass withdrawal. Two areas of peak are identified as highlighted by broken lines. (c) Normal stress change on LRF. (d) Shear stress change on LRF. Grey point indicates maximum stress change. Black point indicates the projection of hypocenter location determined by Delouis *et al.* (2021) on LRF.

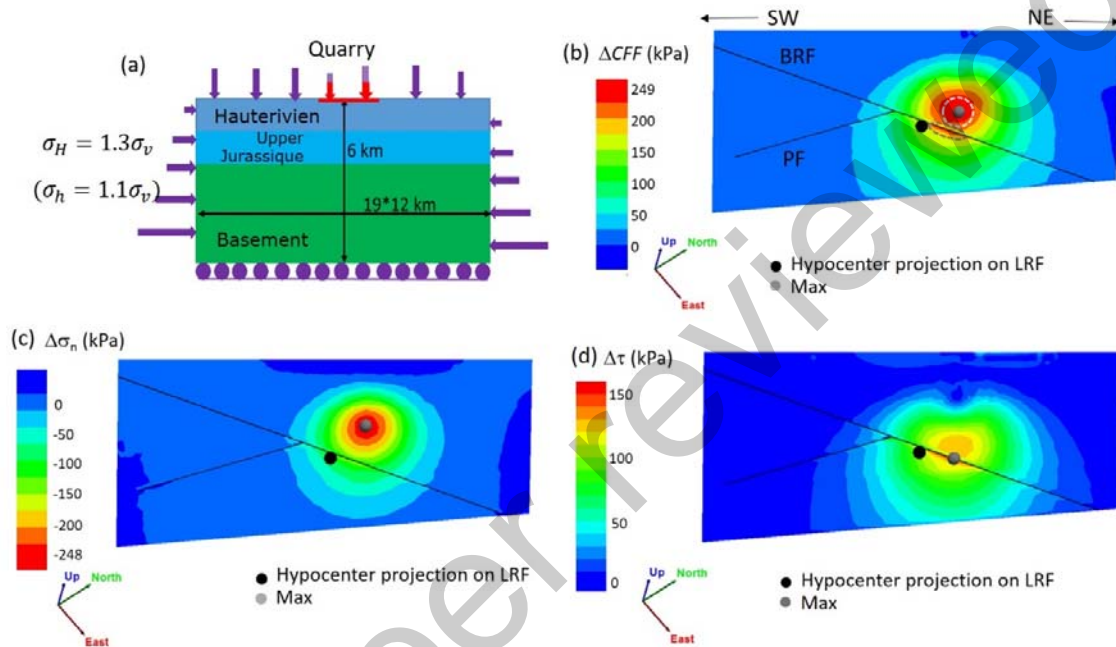
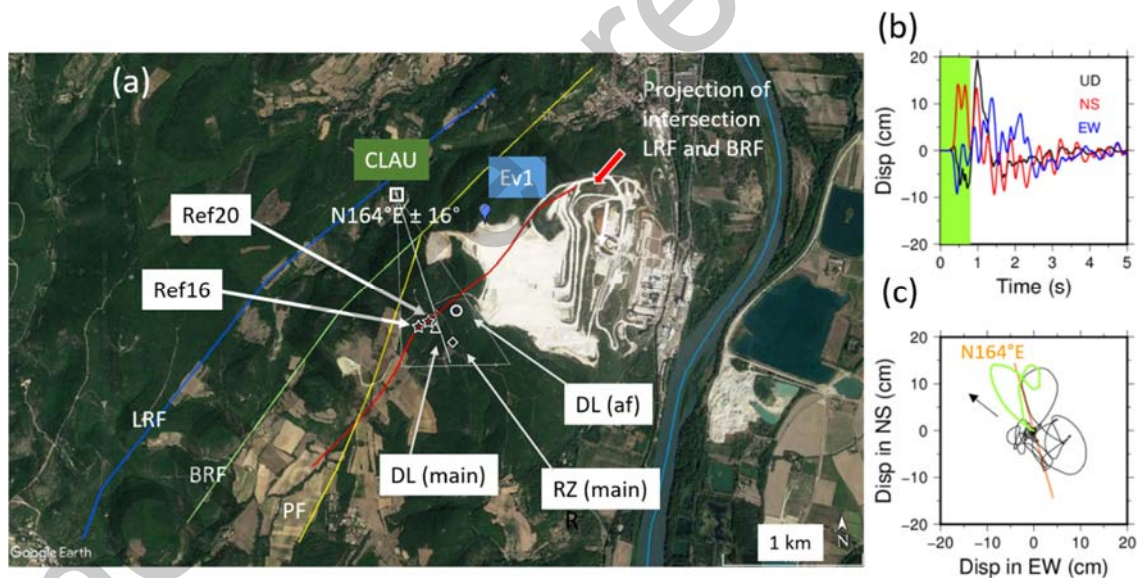


Figure 9. Comparison of different epicenter locations of Le Teil earthquake. (a) Ref16 and Ref20 (stars) are the locations of maximum overpressures calculated by both reference cases Ref16 and Ref20. The red line represents the surface projection of the intersection at depth between LRF and BRF. Ev1 is the location of the blast event of 25th September 2019 in the quarry that is used in the analyses (Method section). DL (main): Epicenter location (triangle) of the mainshock suggested by Delouis et al. (2021). RZ (main): Epicenter location (losange) suggested by Ritz et al. (2020). DL (af): Epicenter location (circle) of the aftershock (MI 2.8) of the 23 November 2019 suggested by Delouis et al. (2021). Also shown is the sensor at the private Clauzel house (CLAU) located between LRF and BRF. (b) Waveforms in displacement of the earthquake event recorded by the sensor CLAU (integrated once from original record in velocity). The three components are displayed (NS, EW, UD). (c) Horizontal particle motion for the selected time window of the beginning of the signals (shown in panel (b) with green color) and associated polarity (orange line).



Supplementary Information to “Double surface rupture and hydraulic recharge of a three-fault system during the Mw 4.9 earthquake of 11 November 2019 at Le Teil (France)”

André Burnol^{1*}, Antoine Armandine Les Landes¹, Daniel Raucoules¹,
Michael Fournelis¹, Cécile Allanic¹, Fabien Paquet¹, Julie Maury¹, Hideo
Aochi¹, Théophile Guillon¹, Mickael Delatre¹, Pascal Dominique¹, Adnand
Bitri¹, Simon Lopez¹, Philippe P. Pébay², Behrooz Bazargan-Sabet¹

1. BRGM, 3 avenue Claude Guillemin, BP 36009, 45000 Orléans, France

2. Eredio, 28 rue de la Plane, 84330 Le Barroux

*Corresponding Author.

Email: a.burnol@brgm.fr

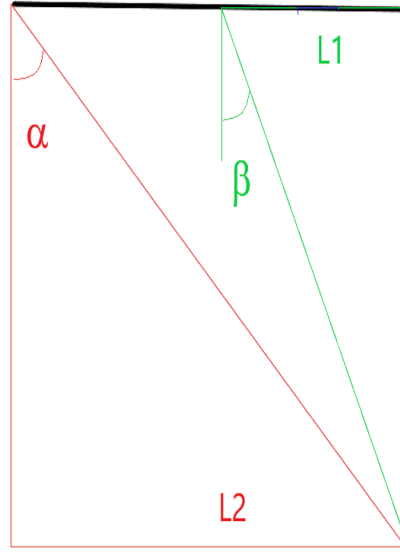
This file contains:

Texts S1-S3,

Tables S1-S4,

Figures S1-S9.

Text S1: Geometry of a two-fault system using a seismic profile.



The Two-way traveltimes (TWT) result of a seismic profile is often not adequate to measure the true dip angle of one single fault due to the variations of the velocity with depth. If the lateral velocity variations are small compared to the variations with depth, we can use the ratio of apparent dip angles of a two-fault system in order to calculate both true dip angles.

Alpha (α) and Beta (β) are the supposed constant deviation to the vertical of La Rouvière fault (LRF) and Bayne Rocherenard fault (BRF), respectively.

L1 (and L2) is the horizontal distance between the projection of the intersection point of both faults and the intersection of LRF (and BRF) with the ground surface.

There is a simple trigonometric relationship between these four parameters:

$$\frac{\tan \beta}{\tan \alpha} = \frac{L1}{L2} \quad (1)$$

The equation to solve is therefore:

$$\frac{\tan x}{\tan \mu * x} = \lambda \quad (2)$$

With :

- the unknown x that is the deviation to vertical of BRF
- μ (μ) the ratio between alpha and beta
- λ (λ) the ratio between L1 and L2

We develop a python program using the Newton algorithm to resolve this equation for a couple of values (μ , λ) given by the seismic M201 profile (see Figure 4).

If $\mu = 4$, there is an explicit solution:

$$(\tan x)^2 = 3 - 2\lambda - 2\sqrt{1 + (\lambda - 1)^2} \quad (3)$$

If μ value is less than 4, the Newton method is applied using a first estimate corresponding to the explicit solution obtained with $\mu = 4$ (see text S2).

Text S2: Python script to resolve the equation (2)

```
#!/usr/bin/env python3

"""
:author: André Burnol
:date: 08 avril 2021
"""

from math import tan, atan, cos, sqrt, pi

def beta4rad(l):
    """fonction inverse de  $l = \tan(x)/\tan(4x)$ 

    x=0 if l=1/4
    """
    return atan(sqrt(3 - 2 * l - 2 * sqrt(l**2 - 2 * l + 2)))

def beta4(l):
    """fonction inverse de  $l = \tan(x)/\tan(4x)$ 

    x=0 if l=1/4
    """
    return 180 * beta4rad(l) / pi

def betarad_from_mu_lambda(mu, l):
    """fonction inverse de  $l = \tan(x)/\tan(\mu * x)$ 

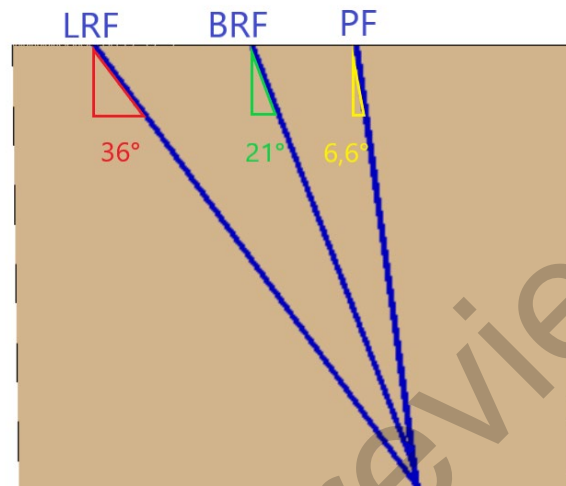
    x=0 if l=1/mu
    """
    x0 = 4/mu * beta4rad(mu * 1/4)
    x = x0
    epsilon = 1e-14 # objectif en erreur relative
    delta = - (tan(x)-l*tan(mu*x))/(1/cos(x)**2-mu*l/cos(mu*x)**2)
    while abs(delta) > epsilon * abs(x):
        x = x + delta
        # méthode de Newton pour résoudre  $\tan(x) - l * \tan(\mu * x) = 0$ 
        delta = - (tan(x)-l*tan(mu*x))/(1/cos(x)**2- mu*l/cos(mu*x)**2)
    return x

def beta_from_mu_lambda(mu, l):
    """fonction inverse de  $l = \tan(x)/\tan(\mu * x)$ 

    if lambda=l=0.5128 and mu=1.76
    >>> beta_from_mu_lambda(1.76, 0.5128)
    20.55150781493907
    >>> beta_from_mu_lambda(1.76, 0.5128)*1.76
    36.170653754292765
    >>> beta_from_mu_lambda(1.76, 0.5128)/3.1
    6.629518649980345
    """
    return 180 * betarad_from_mu_lambda(mu, l) / pi
```

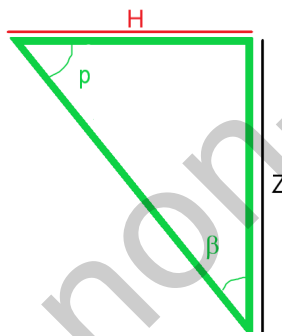
Text S3: Application to the three-fault system using M201 seismic profile and comparison with the observations of SC03 geotechnical drilling

From the M201 seismic profile (see Figure 4), we found $(\mu, \lambda) = (1.76, 0.5128)$ and the solution given by the $\beta_{\text{from_mu_lambda}}(\mu, \lambda)$ is $\beta = 21^\circ$ and therefore $\alpha = \mu * \beta = 36^\circ$. The same method is used for the Paurière fault (PF), we found using M201 profile a ratio of both angles of $\mu_2 = 3.1$ and therefore the deviation of PF to the vertical is $\beta / 3.1 = 6.6^\circ$.

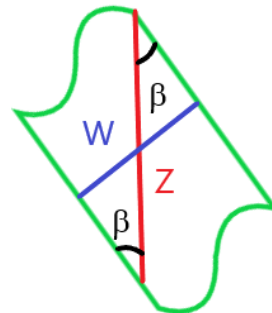


The corresponding dip angles of LRF, BRF and PF are therefore 54° , 69° and 83.4° (Figure 4c).

Another way to calculate the deviation to the vertical of BRF is to use the observations of SC03 geotechnical drilling conducted in 2016 by the quarry owner (see Figure S5 below):



$$\tan \beta = \frac{H}{Z} \quad (4)$$



$$Z \times \sin \beta = W \quad (5)$$

In Figure S5, the photo S5b of SC03 core reveals a natural sub-vertical fracture at 90.5m vertical depth (with calcite veins). By using $(H, Z) = (35.6 \text{ m}, 90.5 \text{ m})$, we found $\beta = 21.47^\circ$ using (4). Both values of the dip angle of BRF we found are therefore consistent and credible if it assumed that this dip angle is laterally and vertically constant. Using this β value, we can estimate the thickness of BRF noted W by supposing that the height Z of (5) is located between a depth of approximately 83 m to 115 m (see Figure S5): $W = 32 \text{ m} * \sin (21.47^\circ) = 11.7 \text{ m}$. Therefore, a range of values of the width between 10 m and 30 m can be used (see Tables 1 and S4).

- **Supplementary tables**

Table S1: Characteristics of the produced interferograms.

Track ID	Acquisition dates	Perpendicular baseline (m)	Time span (days)
059 (ascending)	6/11/2019 and 12/11/2019	13	6
161 (ascending)	7/11/2019 and 13/11/2019	92	6
037 (descending)	11/11/2019 and 17/11/2019	7	6
139 (descending)	6/11/2019 and 12/11/2019	51	6

Table S2: fault parameters after Derode et al (2015) used for 3DECTM simulation.

Parameters	Values
Normal stiffness k_n [GPa/m]	20
Shear stiffness k_s [GPa/m]	20
Friction coefficient μ	0.6

Table S1 : Model parameters of the medium for 3DECTM simulation. Thickness represent the value below le Teil. Each layer is inclined slightly of 3° to 5°.

Parameters	Value		
	Hauterivian	Upper Jurassic	Basement
Poisson ratio ν	0.24	0.27	0.3
Young modulus E [GPa]	42	16	61
Density [kg/m ³]	2500	2600	2690
Thickness [m]	420	780	-

Table S4: ComPASS results for a 10-fold decrease of the fault permeability and fault porosity compared to the reference cases (Table 1).

	Ref6	Ref19
Soil moisture	SM30 (Berzème, 30 cm depth)	SSM (SMOS DES, 10 days)
Matrix Porosity w_m	0.2	0.2
Matrix Permeability K_m	10^{-18} m^2 in Apto-albien	10^{-18} m^2 in Apto-albien
	10^{-16} m^2 elsewhere	10^{-16} m^2 elsewhere
Fault Porosity w_f	0.01	0.01
Fault Permeability K_f	10^{-12} m^2	10^{-12} m^2
Fault Width W	20 m	20 m
Maximum differential of pressure (ΔP) along the intersection LRF / BRF	9.6 bar	7.3 bar

- **Supplementary Figures**

Figure S1: position of our interpretation of the A059 interferogram on the 1:50 000 geological map (Kerrien et al., 1989). Black lines (solid and dotted): the position of the faults resulting from the geological map. Blue lines: our rupture lines based on the DInSAR results. Red dots: the observations of surface ruptures from Ritz et al. (2020).

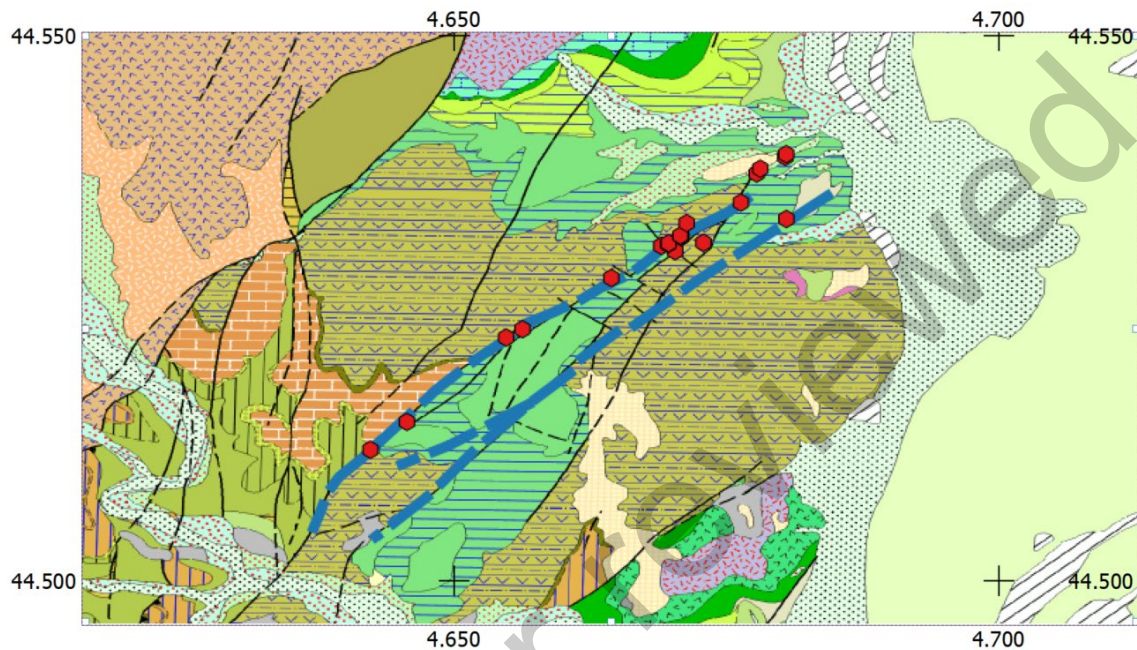


Figure S2: example of use of the Cosi-corr's profiles stacking tool. Left: interferogram A059 as represented in Cosicorr: red line fault "candidate" for LRF, yellow area containing the 10 profiles to be stacked (1500m X 150m). Right: stacked profile across LRF (position in pixels – i.e. 15m – displacement values in meters). Displacement on the fault is automatically computed as the difference at 0 position between the 2 green lines (linearly fitting the motion each side of the fault).

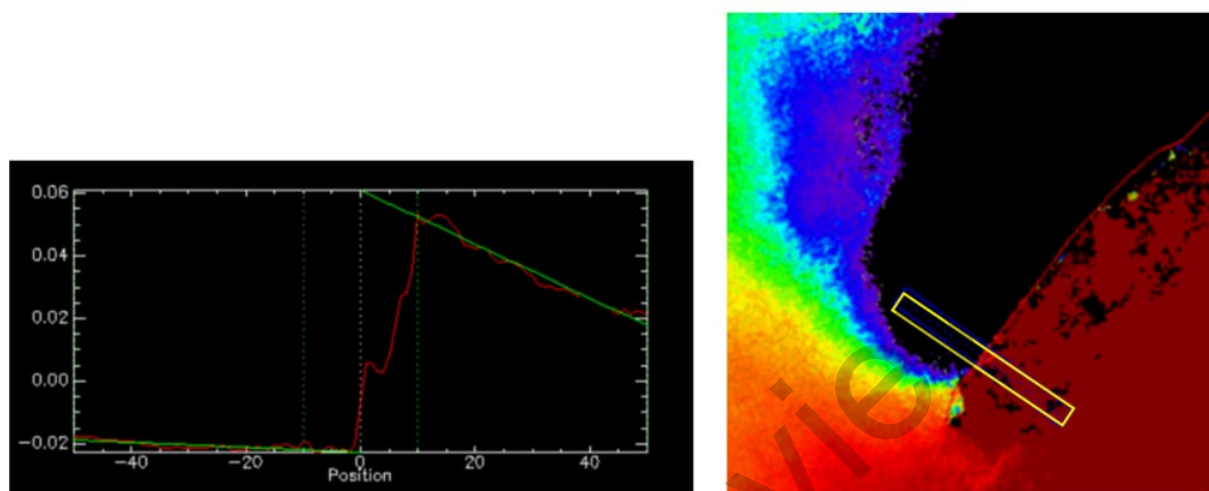


Figure S3: Diagram illustrating (in a very simplified way) a specific unwrapping issue due to two parallel jumps (in our case two surface ruptures represented by F1 and F2). Red line is a profile on the original wrapped interferogram. Assuming that the displacement should be zero at $\pm\infty$ left part of F1 and right part of F2 can be unambiguously unwrapped (blue dashed line). However between F1 and F2 the unwrapping solution results ambiguous: on solution a) all the displacement is on F2, on solution b) all the displacement is on F1, intermediary solutions are possible (e.g. c))

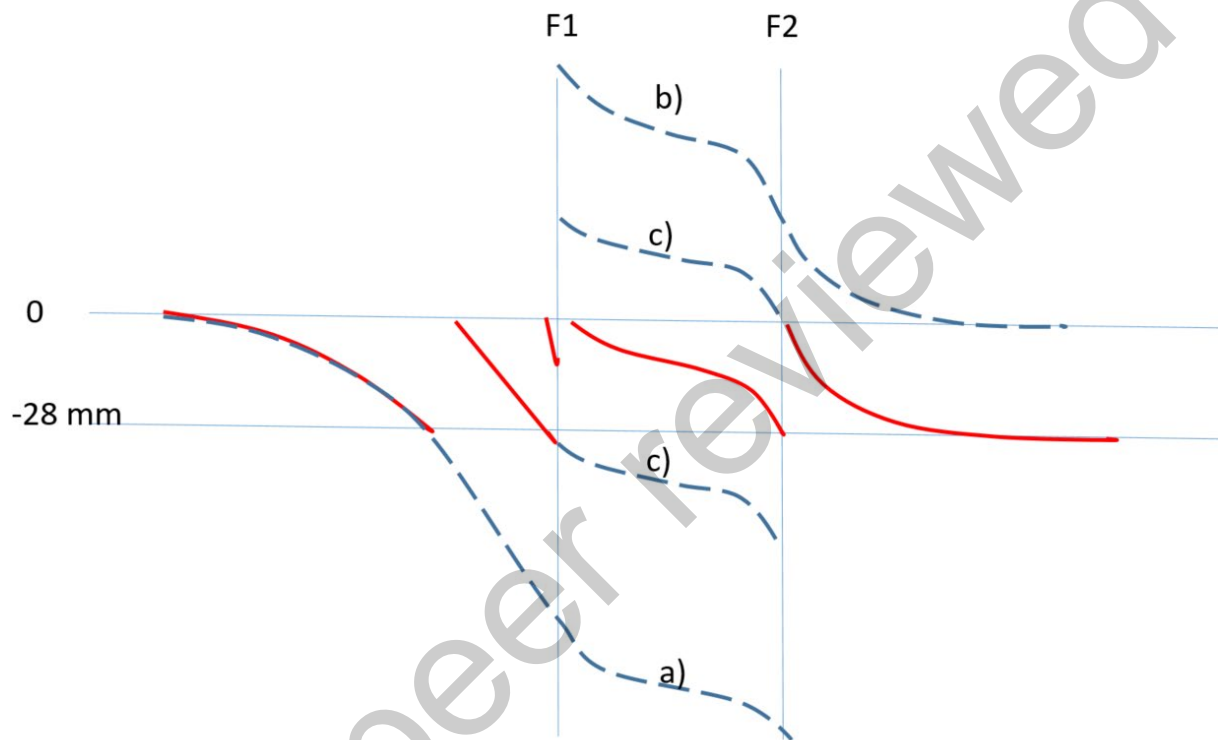


Figure S4: comparison of our unwrapped interferogram (A) with the figure (B) adapted from Ritz et al. (2020) on the North-East sector of the area of interest. We can observe that the unwrapping algorithms have distributed differently the slips between the two ruptures. For instance in Ritz et al. (2020) the LRF is locally locked suggesting a more complex behavior than in our interpretation (where this lock is not significant).

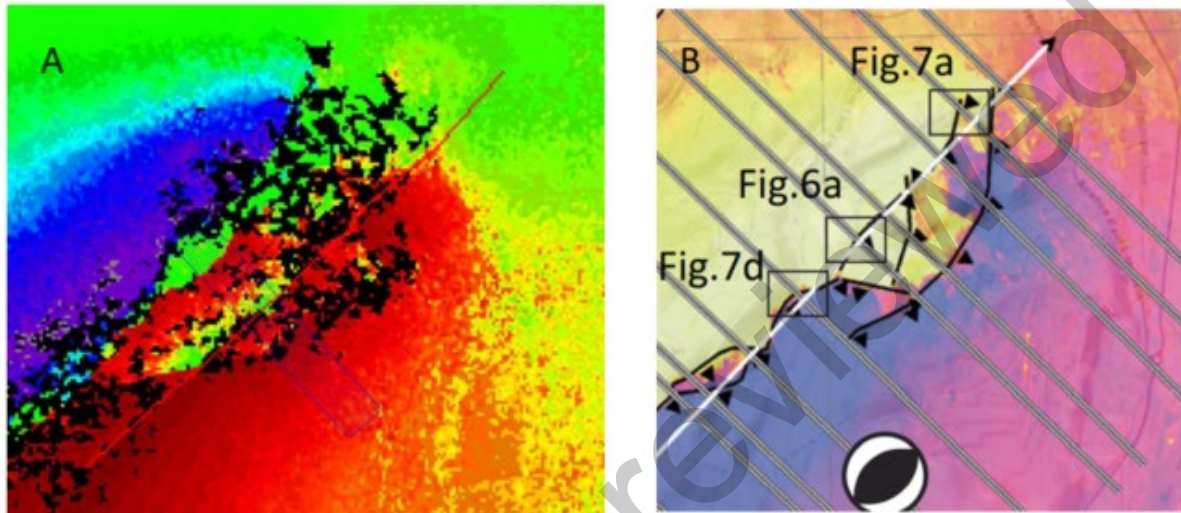


Figure S5: SC03 geotechnical drilling conducted in 2016 by the quarry owner: a) location of SC03 about 35.6 m (red line) southeast of Bayne Rocherenard fault (yellow line near P0) b) core samples at depth between 89 m and 92 m, c) core samples at depth between 112.5 m and 115.3 m.

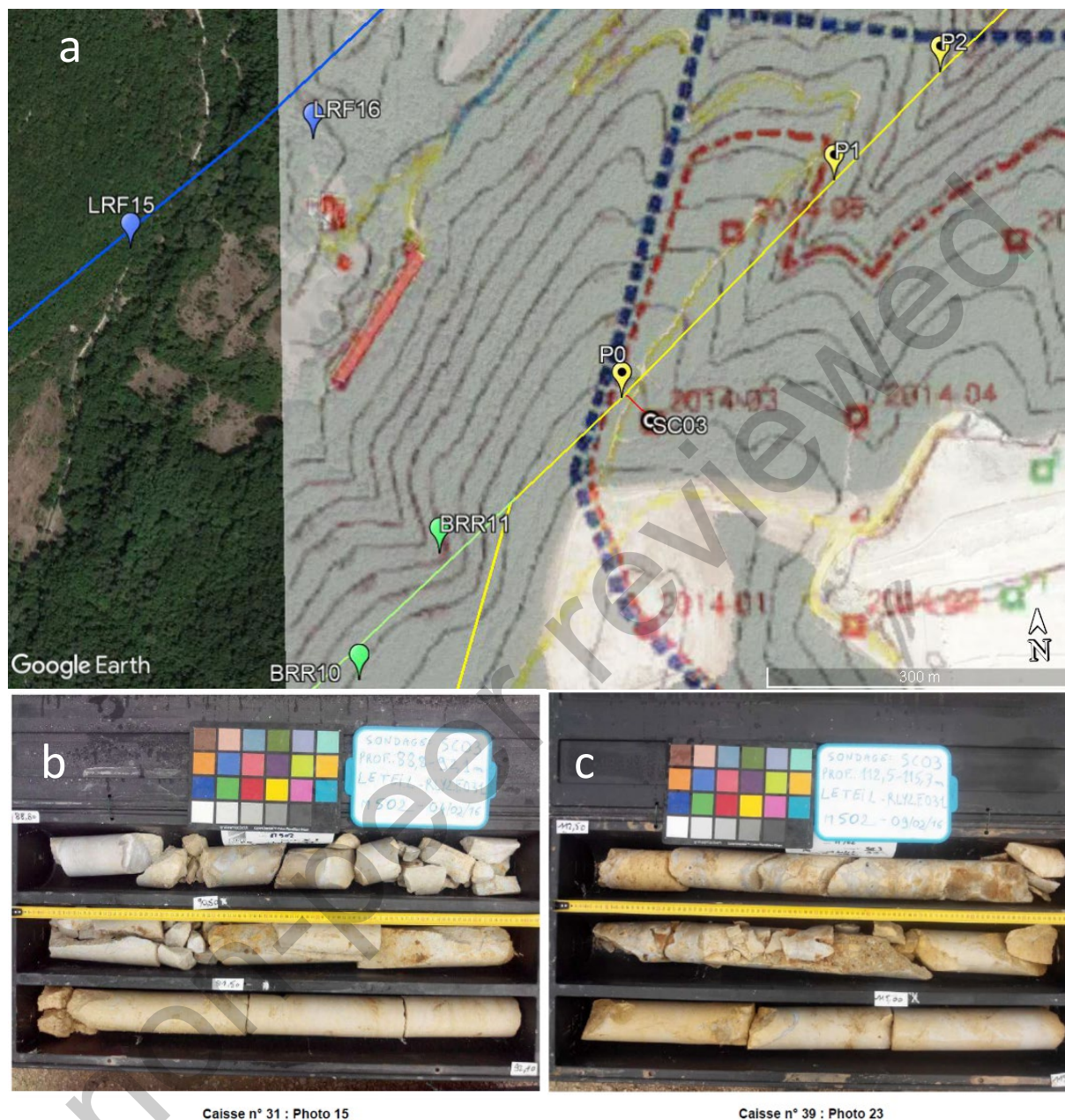


Figure S6: (a) Regional setting with both SMOS cells L1 and L2 around Le Teil. The rainfall station is located in L2, the soil moisture station (Berzème) from the SMOSMANIA network in L1 and the Valvignères borehole in L1. The location and the date of all the seismic events in the area of 50 km x 25 km (L1 and L2) recorded by the French national catalogue (RénaSS) are shown during the 2010-2019 period. (b) Comparison of the rainfall data with the Soil Moisture (SM) at Berzème (1 day) and the Surface Soil Moisture (SSM) acquired by SMOS (descending path, 10 days) during the 2010-2019 period. (c) Cell pressure (blue line) and cell pressure gradient (dotted green line) in the Ref19 case (Table S4) using the Surface Soil Moisture (SSM) acquired by SMOS (descending path, 10 days) during the period 2010-2019.

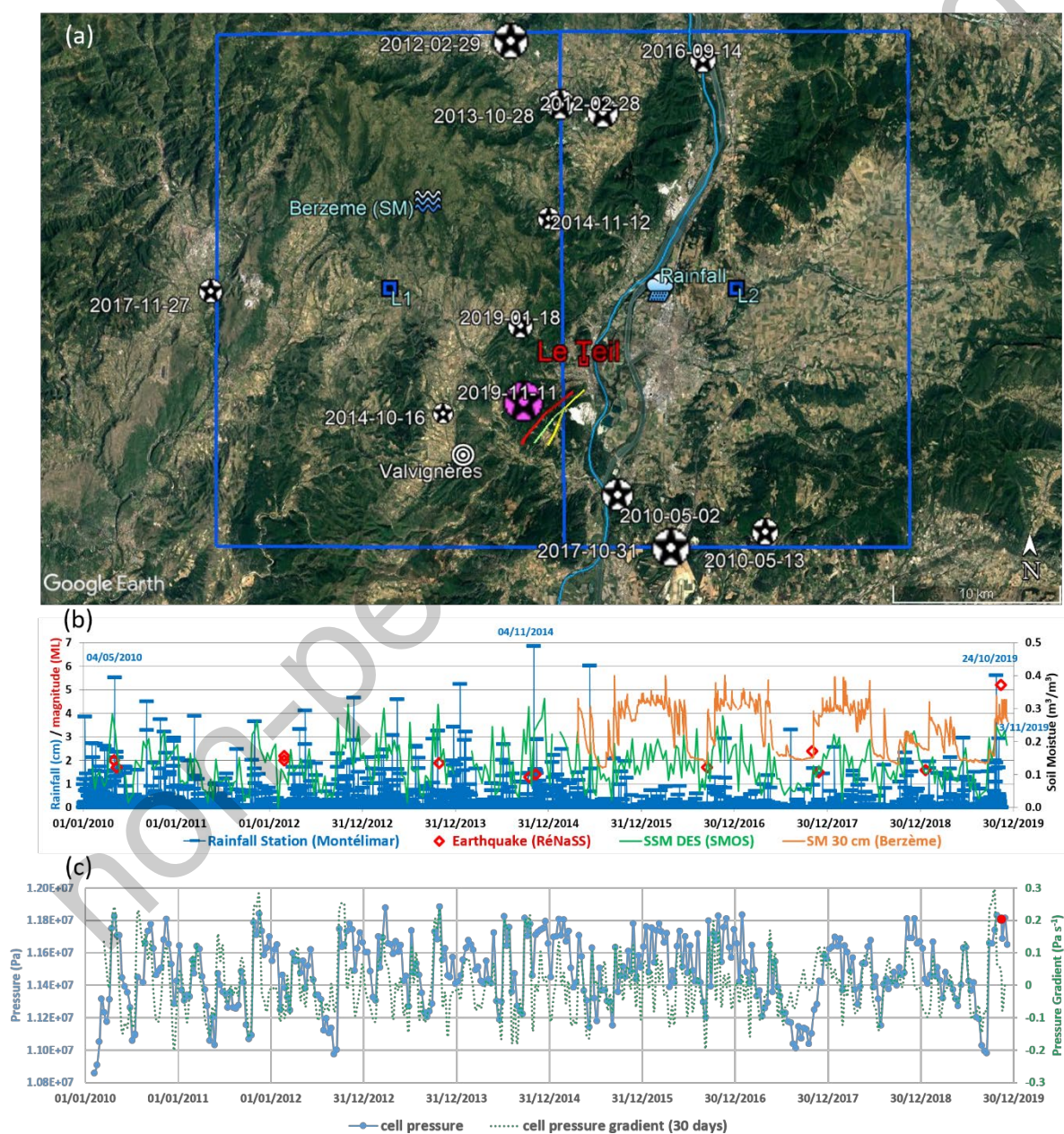


Figure S7: Fault models and numerical meshes in 3DEC simulations. The dimension (x,y,z) is 19 km (N110°E) x 12 km (N20°E) x 6 km (vertical). (a) Fault elements implemented in simulation. (2) A snapshot of simulation in a fault system with respect to the surface quarry. The color indicates the ΔCFF , whose color scale is indicative.

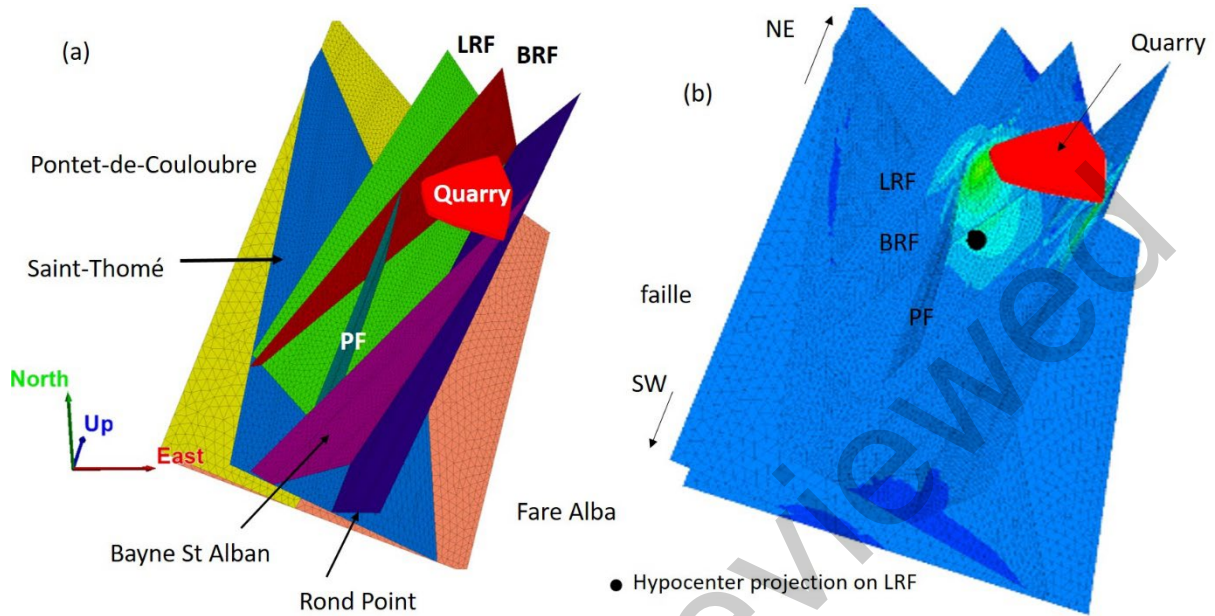


Figure S8: Estimated extracted area and topography change between 1833-2019. The earlier period before 1950 is based on the estimation of De Novellis et al. (2020) and the extracted volume is evenly distributed on the corresponding surface. The extracted volume during the second period after 1950 is estimated from the topography change observed on map.

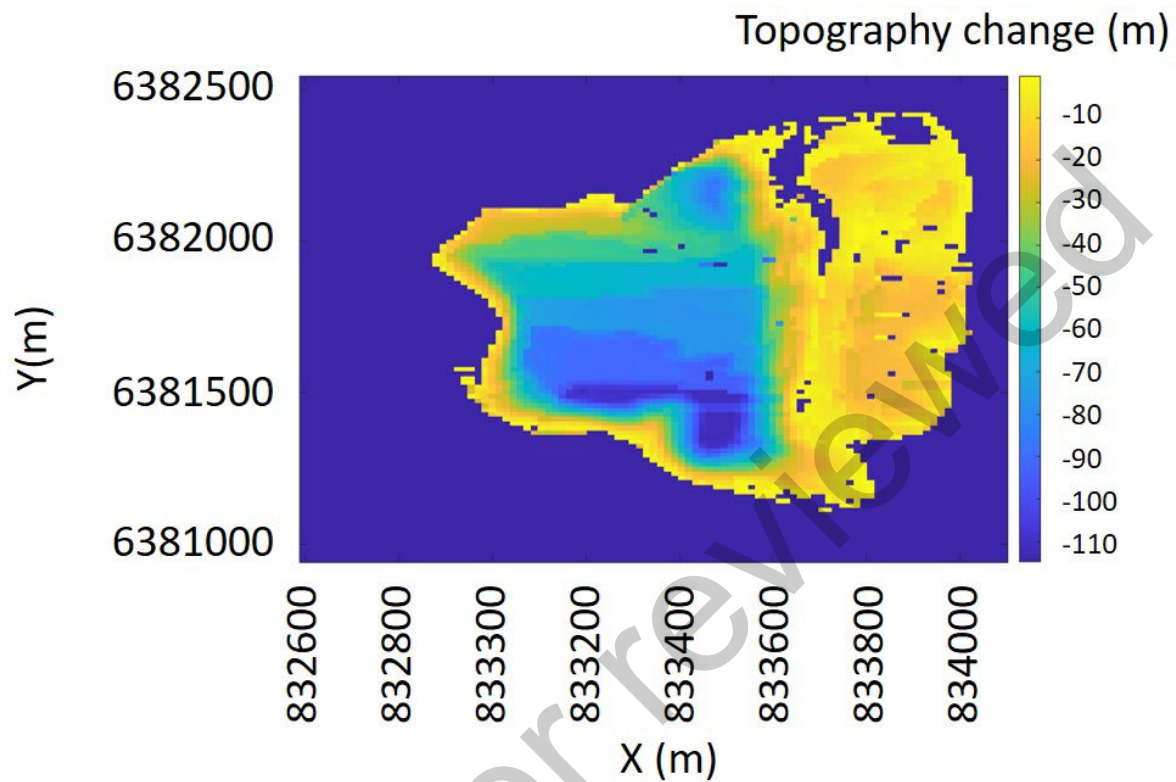
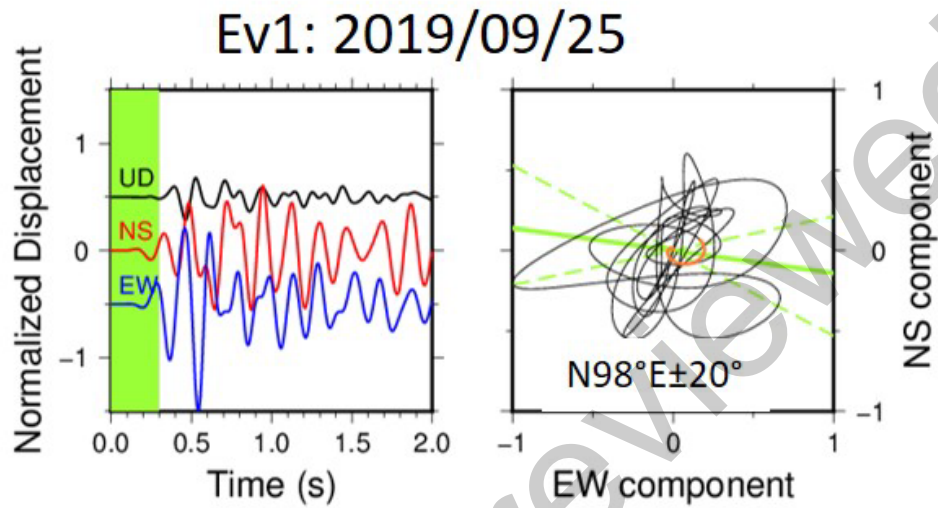


Figure S9: Ground motion recorded at Clauzel house (CLAU) for the blast event of the 25th September 2019. Filtered (1-10 Hz) and integrated seismograms in the left panel. The horizontal particle motion at the right. The first 0.3 second is highlighted as red line. The azimuth is estimated to $N98^{\circ}E \pm 20^{\circ}$ (green line with broken lines) with respect to the true value of $N111^{\circ}E$.



- **References**

Derode, Benoit, Yves Guglielmi, Louis De Barros, et Frédéric Cappa. « Seismic responses to fluid pressure perturbations in a slipping fault ». *Geophysical Research Letters* 42, n° 9 (16 mai 2015): 3197-3203. <https://doi.org/10.1002/2015GL063671>.

Y Kerrien, S Elmi, R. Busnardo, G. Camus, G. Kieffer, J. Moinereau, A. Weisbrod. « Carte géol. France (1/50000), feuille Aubenas (865). BRGM : Orléans. Notice explicative par S. Elmi, R. Busnardo, B. Clavel, G. Camus, G. Kieffer, P. Bérard, B. Michaëly (1996), 170 p. » Orléans: BRGM, 1989.

Ritz, Jean-François, Stéphane Baize, Matthieu Ferry, Christophe Larroque, Laurence Audin, Bertrand Delouis, et Emmanuel Mathot. « Surface rupture and shallow fault reactivation during the 2019 Mw 4.9 Le Teil earthquake, France ». *Communications Earth & Environment* 1, n° 1 (27 août 2020): 10. <https://doi.org/10.1038/s43247-020-0012-z>.

De Novellis, Vincenzo, Vincenzo Convertito, Sotiris Valkaniotis, Francesco Casu, Riccardo Lanari, Mario Fernando Monterroso Tobar, et Nicola Alessandro Pino. « Coincident locations of rupture nucleation during the 2019 Le Teil earthquake, France and maximum stress change from local cement quarrying ». *Communications Earth & Environment* 1, n° 1 (18 septembre 2020): 20. <https://doi.org/10.1038/s43247-020-00021-6>.